

# A comparison between Shapefit compression and Full-Modelling method with PyBird for DESI 2024 and beyond

Y. Lai<sup>1</sup>, C. Howlett<sup>1</sup>, M. Maus<sup>2</sup>, H. Gil-Marín<sup>3</sup>, H. E. Noriega<sup>3,4,5</sup>, S. Ramírez-Solano<sup>5</sup>, P. Zarrouk<sup>6</sup>, J. Aguilar<sup>7</sup>, S. Ahlen<sup>8</sup>, O. Alves<sup>9</sup>, A. Aviles<sup>4,10</sup>, D. Brooks<sup>11</sup>, S. Chen<sup>12</sup>, T. Claybaugh<sup>7</sup>, T. M. Davis<sup>1</sup>, K. Dawson<sup>13</sup>, A. de la Macorra<sup>5</sup>, P. Doel<sup>11</sup>, J. E. Forero-Romero<sup>14,15</sup>, E. Gaztañaga<sup>16,17,18</sup>, S. Gontcho A Gontcho<sup>7</sup>, K. Honscheid<sup>19,20,21</sup>, S. Juneau<sup>22</sup>, M. Landriau<sup>7</sup>, M. Manera<sup>23,24</sup>, R. Miquel<sup>24,25</sup>, E. Mueller<sup>26</sup>, S. Nadathur<sup>17</sup>, G. Niz<sup>27,28</sup>, N. Palanque-Delabrouille<sup>7,29</sup>, W. Percival<sup>30,31,32</sup>, C. Poppett<sup>2,7,33</sup>, M. Rezaie<sup>34</sup>, G. Rossi<sup>35</sup>, E. Sanchez<sup>36</sup>, M. Schubnell<sup>9,37</sup>, D. Sprayberry<sup>22</sup>, G. Tarlé<sup>9</sup>, M. Vargas-Magaña<sup>5</sup>, L. Verde<sup>3,25</sup>, S. Yuan<sup>38</sup>, R. Zhou<sup>7</sup>, H. Zou<sup>39</sup>

Affiliations are in Appendix F

E-mail: [y.lai@uqconnect.edu.au](mailto:y.lai@uqconnect.edu.au)

**Abstract.** DESI aims to provide one of the tightest constraints on cosmological parameters by analyzing the clustering of more than thirty million galaxies. However, obtaining such constraints requires special care in validating the analysis methods, and efforts to reduce the computational time required through techniques such as data compression and emulation. In this work, we perform a precision validation of the PYBIRD power spectrum modelling code with both a traditional, but emulated, *Full-Modelling* approach and the model-independent *Shapefit* compression approach. Using cubic simulations, which accurately reproduce the clustering and precision of the DESI survey, we find that the cosmological constraints from *Shapefit* and *Full-Modelling* are consistent with each other at the  $\sim 0.3\sigma$  level. Both *Shapefit* and *Full-Modelling* are also consistent with the true  $\Lambda$ CDM simulation cosmology, even when including the hexadecapole, down to a scale  $k_{\max} = 0.20h\text{Mpc}^{-1}$ . For extended models such as the  $w$ CDM and the  $o$ CDM models, we find including the hexadecapole can significantly improve the constraints and reduce the systematic errors with the same  $k_{\max}$ . Furthermore, we also show that the constraints on cosmological parameters with the correlation function evaluated from PYBIRD down to  $s_{\min} = 30h^{-1}\text{Mpc}$  are unbiased, and consistent with the constraints from the power spectrum.

**ArXiv ePrint:** [1234.56789](https://arxiv.org/abs/1234.56789)

---

## Contents

<b>1</b>	<b>Introduction</b>	<b>2</b>
<b>2</b>	<b>Simulated Samples</b>	<b>3</b>
2.1	Mock Samples	3
2.2	Covariance matrix	4
<b>3</b>	<b>Theory</b>	<b>5</b>
3.1	PYBIRD	5
3.2	<i>ShapeFit</i>	6
3.3	Converting <i>ShapeFit</i> parameters to cosmological parameters	7
3.4	Computational efficiency	8
<b>4</b>	<b>Summary of main results</b>	<b>9</b>
4.1	Configuration	9
4.2	Main results	10
<b>5</b>	<b><i>ShapeFit</i> tests</b>	<b>12</b>
5.1	Effect of $k_{\max}$	12
5.2	Including the hexadecapole	13
5.3	Maximum and minimum freedom	16
<b>6</b>	<b><i>Full-Modelling</i> tests</b>	<b>16</b>
6.1	Effect of $k_{\max}$	17
6.2	Including the hexadecapole	20
6.3	Maximum and minimum freedom	21
6.4	Comparing <i>ShapeFit</i> vs <i>Full-Modelling</i>	22
<b>7</b>	<b>Correlation function</b>	<b>22</b>
<b>8</b>	<b>Conclusion</b>	<b>29</b>
<b>A</b>	<b>Co-evolution of PyBird bias parameters</b>	<b>30</b>
<b>B</b>	<b><i>ShapeFit</i> conversion nuances</b>	<b>30</b>
<b>C</b>	<b>Performance of Taylor expansion</b>	<b>31</b>
<b>D</b>	<b>Marginalized vs unmarginalized constraints</b>	<b>32</b>
<b>E</b>	<b>Effect of different PyBird versions.</b>	<b>32</b>
<b>F</b>	<b>Author affiliations</b>	<b>33</b>
<b>G</b>	<b>Data Availability</b>	<b>36</b>

---

# 1 Introduction

The universe’s large-scale structure (LSS) encoded in galaxies’ positions contains valuable information on cosmic growth, which can be used to constrain cosmological parameters. Unlike the Cosmic Microwave Background (CMB) which is an effectively 2-dimensional surface at the last scattering, galaxy surveys can probe the full 3-dimensional spectrum of modes and perturbations in the universe over a much larger volume. This means galaxy surveys can potentially provide tighter constraints on the cosmological parameters than the CMB [1]. However, this is made challenging due to the non-linear growth of structure between the epoch of recombination and now. Recent developments in nonlinear modeling, and particularly in Effective Field Theory models of Large-scale Structure (EFTofLSS; [1, 2]) have enabled us to extract more information from the nonlinear regimes, in such a way that allows current and future surveys to reach their scientific potential.

The Dark Energy Spectroscopic Instrument (DESI) is one such example. DESI [3–9] is forecasted to obtain more than an order of magnitude more galaxies than any previous survey. Although the huge amount of data will provide us with the strongest constraints on cosmological parameters with galaxy surveys to date, it also means that 1) our methodologies require more precise validation than what was necessary for previous surveys; and 2) a much longer computing time is required to analyze the data. The aim of this work, along with a series of other papers to be released coincidentally [10–13], is to perform this validation. We validate methods designed to extract cosmological information by modeling the clustering of galaxies measured with DESI. We also investigate how to reduce the information in the two-point statistics to a smaller set of compressed parameters that are then used for fitting to wider ranges of cosmological models.

In the brute force approach to cosmological parameters, one can consider computing the two-point clustering of galaxies (i.e., the power spectrum) within a certain cosmological model and using the Markov Chain Monte Carlo (MCMC) process to find the range of model power spectra that best-fit a dataset. This process is referred to in this work as “*Full-Modelling*” fitting. There are now many codes on the market to achieve this; within the DESI collaboration, we have been testing four different pipelines: PYBIRD [14–16], VELOCILEPTORS [17, 18], FOLPS $\nu$  [19], and EFT-GSM [20]. However, one of the problems with *Full-Modelling* methods (without emulators) is that they take a (relatively) long time to compute the model power spectrum, so the MCMC is very slow.

To speed up the *Full-Modelling* fitting, we can either shrink the size of the data vector [21] or use emulators [14, 22]. However, *Full-Modelling* fitting is also model-dependent — we have to re-fit the entire set of power spectra when we change the underlying cosmological model. Another widely used compression technique is to fit for parameterized, model-independent, growth and Baryon Acoustic Oscillation (BAO) parameters first and then convert these parameters to cosmological parameters [23–28]. This is called the standard “*Template*” fitting method. It has the benefit of not requiring the underlying clustering to be re-fit for testing different cosmologies, so long as the model of interest does not stray too far from the realm of validity for the template [29, 30].

However, *Template* Fitting has been found to have less constraining power than the *Full-Modelling* method [31, 32] when using constraints from the LSS alone. Recent works [32, 33] demonstrated that the *Template* method can be augmented with an additional shape parameter  $m$ , which measures the tilt of the power spectrum along with the BAO and growth parameters. Then, this parameter is converted to cosmological parameters like the *Template*

fit. Calling this method “*ShapeFit*”, [34] found this additional degree of freedom helps to break the degeneracy between the scalar amplitude and the matter density and gave similar constraints to the *Full-Modelling* methodology with a fixed  $n_s$  and a BBN (Big Bang Nucleosynthesis) prior on  $\Omega_b$ . Crucially, however, they found *ShapeFit* retains its model-independence, so that we do not need to redo the fit to the data power spectrum when we change the cosmological model, potentially overcoming the limitations presented by the large DESI data volume.

Within this context, the aims of this paper are two-fold. Firstly, we validate that the PYBIRD EFTofLSS pipeline can reliably produce cosmological constraints within DESI, with sufficient control of modeling systematics that we can ensure the robustness of upcoming constraints from the Year 1 data release [35]. Secondly, we test whether *ShapeFit* can still get similar constraints to the *Full-Modelling* fit within DESI, such that the main output product of the collaboration can be a simple set of compressed BAO, growth, and shape compressed parameters with which the community can perform their own cosmological inference. This paper forms one in a set of four, each focused on similar tests with the other pipelines mentioned above (VELOCILEPTORS [11], FOLPS $\nu$  [12], and EFT-GSM [13]). A fifth paper in the series [10] compares and contrasts the results across the different pipelines, demonstrating consistency in the precision of DESI cosmological parameter constraints even in the extreme case of a  $200h^{-3}\text{Gpc}^3$  volume, despite different intrinsic modeling assumptions. This result shows without reasonable doubt that different EFT setups agree.

This paper is organized as follows: Section 2 presents the simulations we used to test our pipeline. Section 3 briefly explains the theory behind the PYBIRD model and how we adopted the *ShapeFit* methodology into this ecosystem. Section 4 shows the configurations we used for our tests and the main results of this work. From there, for the interested reader, we dig deeper into the details of the *ShapeFit* and *Full-Modelling* methods (in Sections 5 and 6 respectively), testing various systematic effects and extended cosmological models. In Section 7, we show a brief but representative set of results from the correlation function and compare them to the constraints with the power spectrum. Lastly, we conclude in Section 8.

## 2 Simulated Samples

We use different methods to generate the power spectra and their covariance matrix for our DESI-based mock galaxy catalogs. For the power spectrum, we use the more accurate N-body simulations from the ABACUSSUMMIT simulation suite [36–38]. For the covariance matrix, we use the less accurate but much faster Extended Zel’dovich (EZ) [39] mocks. We calculate the covariance matrix from 1000 EZ mocks.

### 2.1 Mock Samples

Mock catalogues for the Luminous Red Galaxy (LRG), the Emission Line Galaxy (ELG), and the Quasi Steller Objects (QSO) samples in DESI are produced from the ABACUSSUMMIT Simulations with  $6912^3$  particles within a cubic box of  $2000h^{-1}\text{Mpc}$ . These mocks assume a Planck2018 [40] cosmology with  $A_s = 2.083 \times 10^{-9}$ ,  $h = 0.6736$ ,  $\omega_{\text{cdm}} = 0.12$ ,  $\omega_b = 0.02237$ ,  $w = -1.0$ , and  $\Omega_k = 0.0$ . Throughout this work, we will test our method with these cubic box mocks. These mocks do not contain the survey geometry of DESI, but this is appropriate for our model comparisons and tests, as we expect the window function to apply equally regardless of the underlying theoretical model. There are 25 different realizations for the LRG, ELG, and QSO samples. The snapshot redshift is 0.8 for the LRG sample, 1.1 for

the ELG sample, and 1.4 for the QSO sample [41, 42]. The LRG and ELG mocks are further sub-sampled to match the redshift distribution of the LRG [43, 44] and ELG [45, 46] target selections. Ref. [47] gives a more detailed description of the LRG mocks, so we will refer our reader to Section 3 of their paper for more information. Furthermore, [48] and [49] provide more details of the ELG and QSO mocks, respectively. Throughout this paper, if we are fitting a single tracer, we fit the mean of the 25 mocks, resulting in an effectively noise-free measurement of the clustering. If we combine three different tracers, we fit the mean of LRG with the first eight mocks, ELG with the mean of the 9th to the 16th mock, and QSO with the mean of the 17th to the 24th mock. This is done to avoid the cross-correlation between two different tracers built from the same realizations (albeit at different redshifts).

## 2.2 Covariance matrix

The covariance matrices are calculated from the EZ mocks. The EZ mocks extend on the Zel'dovich approximation [50] by including the stochastic scale-dependent, non-local, and nonlinear biasing contributions [39]. The EZ mocks are shown to have very similar average clustering properties as the ABACUSSUMMIT mocks in terms of the one-point, two-point, and three-point statistics [47], and are able to be produced at much cheaper computational cost than the full N-body ABACUSSUMMIT mocks. 1000 EZ mock realizations are produced with a  $2000h^{-1}\text{Mpc}$  cubic box, matching the configurations of the ABACUSSUMMIT mocks. The covariance matrices are calculated from these 1000 mocks. To obtain the unbiased inverse covariance matrix  $\hat{\Psi}$ , we apply both the Hartlap factor [51]

$$\hat{\Psi} = \frac{N_S - N_P - 2}{N_S - 1} \Psi \quad (2.1)$$

and the Percival factor [52]

$$m_1 = \frac{1 + B(N_D - N_P)}{1 + A + B(N_P + 1)} \quad (2.2)$$

to the inverse covariance matrix  $\Psi$ . Here,

$$\begin{aligned} A &= \frac{2}{(N_S - N_D - 1)(N_S - N_D - 4)} \\ B &= \frac{N_S - N_D - 2}{(N_S - N_D - 1)(N_S - N_D - 4)} \end{aligned} \quad (2.3)$$

and  $N_S$  is the number of realizations employed to estimate the covariance matrix,  $N_D$  is the length of the data vector, and  $N_P$  is the number of free parameters in the model. Ref. [53] points out that the Hartlap factor is only an approximation. However, the Hartlap factor is very close to one in our analysis because we have 1000 simulations, so it only has a negligible impact on the constraints. Furthermore, the modified likelihood in [53] is non-Gaussian, so we cannot analytically marginalize over the nuisance parameters (see section 3). Therefore, we decided to use the Hartlap factor in our analysis. We use single box covariance matrices (i.e., corresponding to a volume of  $8h^{-3}\text{Gpc}^3$ ) in this work, which is sufficient to explore the impact on DESI-like volumes for each individual tracer, and the three tracers combined (The total volume is  $24h^{-3}\text{Gpc}^3$ ). Tests using a reduced covariance matrix and the mean measurement of the 25 ABACUSSUMMIT realizations (i.e., corresponding to a volume of  $200h^{-3}\text{Gpc}^3$ ) are reserved for the model comparison paper in this series [10]. When we combine different tracers, we multiply the Hartlap and Percival factors into the individual covariance matrix first and then generate the block-diagonal combined covariance matrix.

### 3 Theory

In this section, we will briefly explain the theory behind PYBIRD and *ShapeFit*. For a more detailed explanation, we will refer the readers to [15, 54] for PYBIRD and [32] for *ShapeFit*.

#### 3.1 PyBird

The Standard Perturbation Theory (SPT) for large-scale structures is widely used historically. Its redshift kernels  $Z_n$  were developed to capture the effect of redshift space distortion (see [55] and references therein). However, the SPT model loses reliability around  $k = 0.1h\text{Mpc}^{-1}$ . Building on this, [54] have derived the equations for the galaxy power spectrum within the EFTofLSS up to one-loop order

$$\begin{aligned}
P_g(k, \mu) &= Z_1(\mu)^2 P_{11}(k) + 2 \int \frac{d^3q}{(2\pi)^3} Z_2(\mathbf{q}, \mathbf{k} - \mathbf{q}, \mu)^2 P_{11}(|\mathbf{k} - \mathbf{q}|) P_{11}(q) \\
&+ 6 Z_1(\mu) P_{11}(k) \int \frac{d^3q}{(2\pi)^3} Z_3(\mathbf{q}, -\mathbf{q}, \mathbf{k}, \mu) P_{11}(q) + 2 Z_1(\mu) P_{11}(k) \\
&\left( c_{ct} \frac{k^2}{k_M^2} + c_{r,1} \mu^2 \frac{k^2}{k_r^2} + c_{r,2} \mu^4 \frac{k^2}{k_r^2} \right) + \frac{1}{\bar{n}_g} \left( c_{\epsilon,1} + c_{\epsilon,2} \frac{k^2}{k_M^2} + c_{\epsilon,3} f \mu^2 \frac{k^2}{k_M^2} \right) \quad (3.1)
\end{aligned}$$

where  $P_{11}$  is the linear power spectrum of Cold Dark Matter (CDM) and baryons, usually obtained from Boltzmann codes such as CLASS [56] or CAMB [57, 58]. Different from the SPT model, which does not account for the failure of perturbation theories on small scales, in EFTofLSS, we have the counter terms  $c_{ct}, c_{r,1}, c_{r,2}$  to account for the short wavelength modes. Additionally, we have the stochastic terms  $c_{\epsilon,1}, c_{\epsilon,2}, c_{\epsilon,3}$  to account for the stochastic way in which galaxies trace the underlying matter field and the impact of residual shot-noise on the power spectrum. Lastly,  $f$  is the linear growth rate of structure,  $\mu$  is the cosine of the line-of-sight angle, and  $\bar{n}_g$  is the number density of galaxies in the survey.<sup>1</sup> In addition to the counter terms and stochastic terms, PYBIRD also has 4 bias parameters:  $b_1, b_2, b_3, b_4$  following the West Coast convention of the bias parameters [59]. They enter in the redshift kernel  $Z_n$  calculations. The expressions of the redshift kernels can be found in equation (2.2) of [15]. EFTofLSS requires us to resum the effect of long wavelength displacements with the Lagrangian perturbative treatment [15] to get a more accurate estimation of the galaxy power spectrum. This is because the long wavelength displacement modes cannot be modeled perturbatively. The detail of IR-resummation of EFTofLSS [60] in PYBIRD can be found in Appendix C of [15] and section 4.1 of [16].

To speed up the analysis, PYBIRD analytically marginalizes over all nuisance parameters except  $b_1, b_2$  and  $b_4$ , which are the only parameters that do not enter at linear order in equation (3.1). The marginalized likelihood is given by [15]:

$$\log \mathcal{L} = \frac{1}{2} F_{1,i} F_{2,ij}^{-1} F_{1,j} + F_0 - \frac{1}{2} \ln |\det(F_2)| \quad (3.2)$$

<sup>1</sup>We follow [15] and set  $k_M$  (Inverse tracer spatial extension scale) =  $k_r$  (Inverse velocity product renormalization scale) =  $0.7h\text{Mpc}^{-1}$ . However, the latest version of PYBIRD has the default setting of  $k_M = 0.7h\text{Mpc}^{-1}$  and  $k_r = 0.25h\text{Mpc}^{-1}$ . We found the change in  $k_r$  has little impact on the constraints on Shapefit and cosmological parameters (see Appendix E for more detail).

where

$$\begin{aligned}
F_{2,ij} &= (P_{,b_{G_i}}^W)^T \hat{\Psi} P_{,b_{G_j}}^W \\
F_{1,i} &= (P_{\text{const}}^W)^T \hat{\Psi} P_{,b_{G_i}}^W + P_d^T \hat{\Psi} P_{,b_{G_i}}^W \\
F_0 &= -\frac{1}{2} (P_{\text{const}}^W)^T \hat{\Psi} P_{\text{const}}^W + (P_{\text{const}}^W)^T \hat{\Psi} P_d - \frac{1}{2} P_d^T \hat{\Psi} P_d,
\end{aligned} \tag{3.3}$$

and

$$\begin{aligned}
P_{,b_{G_i}}^W &= \left. \frac{\partial P^W}{\partial b_{G_i}} \right|_{b_G \rightarrow 0}, \\
P_{\text{const}}^W &= P^W \Big|_{b_G \rightarrow 0},
\end{aligned} \tag{3.4}$$

with  $b_G \vec{=} \{b_3, c_{ct}, c_{r,1}, c_{r,2}, c_{\epsilon,1}, c_{\epsilon,2}, c_{\epsilon,3}\}$ .  $P^W$  denotes the model power spectrum ( $P_g$ ) after convolving with the survey window function, and  $\hat{\Psi}$  is the inverse covariance matrix after being multiplied by the Hartlap factor in equation (2.1) and the Percival factor in equation (2.2). Fig. 18 in Appendix D demonstrates numerically that the unmarginalized likelihood gives the same constraints on cosmological parameters as the marginalized likelihood with the mean of the LRG mocks, so for the remainder of this work, we consider only the analytically marginalized constraints.

### 3.2 *ShapeFit*

Unlike the *Full-Modelling* method, *ShapeFit* first compares the data power spectrum (measured assuming a fiducial redshift to distance relationship) to a template power spectrum generated from a chosen set of template cosmological parameters (noting that the template and fiducial cosmological parameters do not have to be the same, but are usually set to be for ease of analysis). By shifting the template in specific ways, we can then constrain more model-independent parameters  $\alpha_{\perp}$ ,  $\alpha_{\parallel}$  (which primarily act to shift and stretch the BAO wiggles of the template power spectrum),  $f\sigma_{s8}$  (which changes the ratio of the amplitude of multipoles in the power spectrum),  $m$  (which changes the slope of the power spectrum) [32].<sup>2</sup> These four parameters will be referred to as the *ShapeFit* parameters from hereon.

As a second step, we can use our knowledge of the fiducial and template cosmological parameters to convert the *ShapeFit* parameters to constraints on the truth cosmological parameters encoded in the data. To do this, we start with the definitions of the *ShapeFit* parameters [33]:<sup>3</sup>

$$\alpha_{\perp} = \frac{D_M r_d^{\text{tem}}}{D_M^{\text{fid}} r_d}, \tag{3.5}$$

$$\alpha_{\parallel} = \frac{H^{\text{fid}}(z) r_d^{\text{tem}}}{H(z) r_d}, \tag{3.6}$$

<sup>2</sup>There is another *Shapefit* parameter  $n$  which also changes the slope of the power spectrum. However,  $n$  only quantifies the changes in slope due to different scalar indices  $n_s$ . Since we fix  $n_s$  in our analysis, we do not include  $n$  in this work.

<sup>3</sup>The “ $f\sigma_{s8}$ ” parameter is actually  $f\sigma_{s8} \approx r_A (f\sigma_{s8})^{\text{tem}} \times \exp\left(\frac{m}{2a} \tanh\left(a \ln\left(\frac{r_d^{\text{tem}}}{8}\right)\right)\right)$  because  $m$  not only changes the tilt of the power spectrum, but also the amplitude. Therefore, if we integrate over the power spectrum, we get this extra exponential factor from integration by parts. However, we only use the amplitude at the pivot scale during the conversion. Equation (3.8) demonstrates  $m$  will not change the amplitude at the pivot scale, so we do not need to multiply this extra factor during the conversion [32, 33].

$$\begin{aligned}
f\sigma_{s8} &= \frac{(f\sigma_{s8})^{\text{tem}}}{\left(f(P_{\text{lin}}(k_p))^{1/2}\right)^{\text{tem}}} f\left(\frac{1}{s^3}P_{\text{lin}}(k_p/s)\right)^{1/2} \\
&= r_A(f\sigma_{s8})^{\text{tem}},
\end{aligned}
\tag{3.7}$$

and

$$\ln\left(\frac{P(k)}{P^{\text{tem}}(k)}\right) = \frac{m}{a} \tanh\left[a \ln\left(\frac{k}{k_p}\right)\right] + n \ln\left(\frac{k}{k_p}\right),
\tag{3.8}$$

$$s = \frac{r_d}{r_d^{\text{tem}}}.
\tag{3.9}$$

Here,  $P_{\text{lin}}$  denotes the linear power spectrum,  $r_d$  is the sound horizon at the drag epoch,  $D_M$  is the angular diameter distance,  $H$  is the Hubble parameter, and the pivot scale  $k_p \approx \frac{\pi}{r_d} \approx 0.03h\text{Mpc}^{-1}$ . We follow [32] to set  $a = 0.6$ , and  $n = 0$  because we fix the tilt of the primordial power spectrum  $n_s$ . The unit for  $D_M, H(z)$ , and  $r_d$  are all in  $h^{-1}\text{Mpc}$ . Lastly, ‘‘fid’’ here denotes the fiducial cosmology used to convert the redshift to distances, and ‘‘tem’’ denotes the template cosmology used to generate the template power spectrum.

Without using the emulators or Taylor expansion, the first advantage of *ShapeFit* over *Full-Modelling* fit is that *ShapeFit* does not require recalculating the linear matter power spectrum for each iteration of MCMC. Furthermore, although the scaling term in the right-hand-side of equation (3.8) depends on  $k$ . It has been shown in [32] that the scaling terms can be taken out of the loop integrals. Therefore, we can simply multiply the scaling terms by the template loop terms to get the new ones similar to scaling the power spectrum with  $\sigma_8$  (see equation (3.9) of [32] for more detail). In PYBIRD, the IR-resummation terms are also separated based on their loop order. Therefore, we can easily multiply the scaling factor in equation (3.8) to the template IR-resummation terms to get the new ones. Lastly, the first step of *ShapeFit* is model-independent, so we only have to assume the cosmological models when we convert the *ShapeFit* parameters to the cosmological parameters. Therefore, if we want to fit different models, we only need to redo the conversion and do not need to repeat the first step.

In PYBIRD, *ShapeFit* is implemented as follows. Firstly, we generate the linear power spectrum from CLASS [56] or CAMB [57] using the template cosmological parameters. We then compute and store the loop terms of the power spectrum with one-loop EFTofLSS and the IR resummation terms. For each iteration, MCMC will propose different *ShapeFit* parameters. We use equation (3.8) to calculate the new linear power spectrum with the new slope  $m$ . This is then used to rescale the template loop and IR resummation terms. Next, we add the IR resummation terms to the linear and loop power spectra. Lastly, we apply the AP (Alcock Paczynski) effect based on the input  $\alpha$  parameters and convolve the window function with the linear and loop power spectra. We repeat the last three steps for each MCMC iteration until the chain converges.

### 3.3 Converting *ShapeFit* parameters to cosmological parameters

We first need to determine the desired cosmological model before converting *ShapeFit* parameters into cosmological parameters. In this work, we will use PYBIRD to constrain parameters in the  $\Lambda\text{CDM}$ ,  $w\text{CDM}$ , and  $o\text{CDM}$  models. For all models, we put a flat prior on all cosmological parameters except a Big Bang Nucleosynthesis (BBN) prior on  $\omega_b$ . The detail of the priors is in section 4.1. After setting the prior, we compute the covariance matrix ( $C$ )



and the mean  $q_{\text{mean}}$  of the *ShapeFit* chains with CHAINCONSUMER [61] after removing the burn-in. We constrain the cosmological parameters with the Bayesian approach with the log-likelihood function given by

$$\log \mathcal{L} = -\frac{1}{2}(q - q_{\text{mean}})C^{-1}(q - q_{\text{mean}})^T. \quad (3.10)$$

This likelihood function assumes the posterior of the *Shapefit* parameters are Gaussian. The posteriors of the cosmological parameters are found via MCMC. For each iteration, we use CLASS to find  $r_d, D_M(z), H(z), P_{\text{lin}}$ , and NBODYKIT [62] to find  $T_{\text{lin}}^{\text{NW}}$  (the no-wiggle transfer function) based on the proposed cosmological parameters. The  $\alpha$  parameters are found with equation (3.5) and (3.6).  $f\sigma_{88}$  can be found by computing equation (3.7). Lastly, the slope of the power spectrum is given by

$$m = \frac{d}{d \ln k} \left( \frac{(T_{\text{lin}}^{\text{NW}})^2}{s^3 (T_{\text{lin}}^{\text{NW, fid}})^2} \right) \Big|_{k_p}. \quad (3.11)$$

There are three different ways of calculating the no-wiggle transfer function. First is through the Eisenstein-Hu fitting formula [63]. This is calculated through the NBODYKIT package. The second is through the polynomial fitting formula in [64]. The third is through the spectral decomposition from [65, 66]. Appendix B shows that these three de-wiggle algorithms give consistent results.

The conversion assumes the posteriors of the Shapefit parameters are Gaussian distributed. However, section 4 illustrates that the posteriors are generally non-Gaussian. To solve this problem, our code also has the option to use the LINEARNDINTERPOLATOR from SCIPY to interpolate the posterior of the Shapefit chain as the new likelihood during the MCMC. The interpolation will be able to capture the non-Gaussian information. In general, we find consistent constraints with the Gaussian approximation and the linear interpolation methods.

### 3.4 Computational efficiency

Generally, the bottleneck of the *Full-Modelling* methodology is calculating the model power spectrum. To overcome this problem, [14] uses Taylor expansion to approximate the model power spectrum during MCMC. They found the maximum deviation between the Taylor expansion and exact calculation is under 1% for the monopole and 10% for the quadrupole of the power spectrum for the  $\Lambda$ CDM cosmological model with massive neutrinos. They concluded that the errors have a negligible effect on the constraints of cosmological parameters. In this work, we follow [14] to approximate the model power spectrum during the MCMC with a third-order Taylor expansion about models evaluated at equally spaced points within the cosmological parameter space. We verify the accuracy of this method for the  $w$ CDM model in Appendix C, also finding the grid spacing for the Taylor expansion has no impact on our final constraints.

Similarly, the conversion from *ShapeFit* parameters to cosmological parameters can be computationally expensive. To speed this process up, we similarly compute the *ShapeFit* parameters from a grid of cosmological parameters, using the third-order Taylor expansion to interpolate during the MCMC. We find this interpolation gives consistent constraints [10]. The configuration of the grids for the various models we test is described in Section 4.1.

## 4 Summary of main results

We introduce the configurations we used to fit the DESI mocks in this section. We test four different configurations of priors in PYBIRD, and we mainly focus on the “BOSS MaxF” configuration taken from [15]. We then summarise the constraints on cosmological parameters in the  $\Lambda$ CDM model for both *ShapeFit* and *Full-Modelling* with the combination of three tracers, verifying that the two methods return consistent, and unbiased, results at a level suitable for DESI analyses.

### 4.1 Configuration

For *ShapeFit*, the template cosmological parameters used in this work are  $\ln(10^{10}A_s) = 3.0364$ ,  $h = 0.6736$ ,  $\omega_{cdm} = 0.12$ ,  $\omega_b = 0.02237$ ,  $w = -1.0$ , and  $\Omega_k = 0.0$ . These parameters are the same as the fiducial parameters used to make the clustering measurements, and the true cosmological parameters of the ABACUSSUMMIT introduced in Section 2.

The priors we adopt on the cosmological and *ShapeFit* parameters are summarized in Table 1. The Gaussian prior on  $\omega_b$  is chosen to be representative of current results from Big Bang Nucleosynthesis [67]. Four different prior configurations we test for our remaining nuisance parameters are summarized in Table 2. In this work, we mainly use the “BOSS MaxF” and “BOSS MinF” priors taken from [15] with small changes to fit the DESI mocks. The results using the “MaxF” and “MinF” priors where the priors for the counter terms and stochastic terms are completely free, are mainly adopted in the comparison paper [10] to ensure consistent degrees of freedom between different models of the power spectrum. In both “BOSS MinF” and “MinF” configurations,  $b_2, b_3$  and  $b_4$  are calculated using the local Lagrangian approximation [68]. The derivations of these local Lagrangian relations are given in Appendix A.

There are 25 different mocks for each redshift bin from the ABACUSSUMMIT simulation suite. The volume of the ABACUSSUMMIT simulation box is  $8 \text{ Gpc}^3/h^3$ , which is similar to the volume expected for the full DESI survey. As such, we primarily use the covariance matrix corresponding to a single realization (hereon referred to as the single-box covariance matrix) to calculate the possible systematics in the pipeline. Tests using a  $25\times$  reduced covariance matrix (representing the error on the mean) are mainly used to compare the differences between different pipelines in the comparison paper [10]. Doing so enables us to detect if there are any systematics that will affect our measurements at the level of the Year 1 analysis (containing approximately 1/5 of the full DESI data) while avoiding misleading results that may arise from the fact that the simulations are not necessarily converged to a sufficient degree on non-linear scales (i.e., [69], which shows that different simulation codes can differ in their predictions for the power spectrum on non-linear scales at a level comparable to the precision using our  $25\times$  reduced covariance matrix).

Since the LRG, ELG, and QSO mocks are all generated from the same 25 initial conditions, to avoid cross-correlation between different tracers within the same mock, we generate the mean of LRG from the first eight simulations, the mean of ELG from the 9th to the 16th simulations, and the mean of the ELG mocks from the 17th to the 24th simulations. To make a valid comparison between the *ShapeFit* and the *Full-Modelling* method, we also generate the *ShapeFit* constraints from the same mocks. However, when we only fit a single tracer, we fit the mean of the 25 mocks for both *ShapeFit* and *Full-Modelling* as this allows for a more precise test.

Full-Modeling	ShapeFit
$H_0$	$f\sigma_8$
$\mathcal{U}[55.36, 79.36]$	$\mathcal{U}[0, 1]$
$\omega_b$	$\alpha_{\parallel}$
$\mathcal{N}[0.02237, 0.00037]$	$\mathcal{U}[0.9, 1.1]$
$\omega_{\text{cdm}}$	$\alpha_{\perp}$
$\mathcal{U}[0.08, 0.16]$	$\mathcal{U}[0.9, 1.1]$
$\log(10^{10} A_s)$	$m$
$\mathcal{U}[2.0364, 4.0364]$	$\mathcal{U}[-0.4, 0.4]$
$w$	
$\mathcal{U}[-1.5, -0.5]$	
$\Omega_k$	
$\mathcal{U}[-0.25, 0.25]$	

**Table 1.** Priors on the *ShapeFit* and cosmological parameters we use in this work. We use  $\mathcal{U}$  ( $\mathcal{N}$ ) to denote the uniform (Gaussian) prior. The first number is the lower bound (mean), and the second number is the upper bound (standard deviation). The boundaries for the flat priors on cosmological parameters are also the boundaries of the grid used to interpolate the power spectrum.

## 4.2 Main results

Given the above configuration, we start by presenting the main findings of this work. We examine the more nuanced effects (and potential systematics) of fitting to different  $k_{\text{max}}$  scales, with/without including the power spectrum hexadecapole, and of different prior configurations in sections 5 and 6. For Fig 1, 2, 3, and 4 in this section. We use  $k_{\text{max}} = 0.20h\text{Mpc}^{-1}$ , “BOSS MaxF” prior, and without the hexadecapole. To avoid cross-correlation of different redshift bins in the same mock since we didn’t model this in the covariance matrix. We use the mean of mock 1-8 for the LRG analysis, the mean of mock 9-16 for the ELG analysis, and the mean of mock 17-24 for the QSO analysis.

Fig. 1 illustrates the best-fit power spectra from both *ShapeFit* and *Full-Modelling* methods. Both are in good agreement with each other and with the data. The constraints on the cosmological parameters from the *Full-Modelling* power spectrum are shown in Fig. 2. It shows the constraints from *Full-Modelling* with PYBIRD are unbiased relative to the truth values indicated by the dashed lines within  $0.4\sigma$ . The combination of all tracers gives the strongest constraints on the cosmological parameters as expected. PYBIRD can provide unbiased constraints for both the single tracer case and the combination of all tracers. Fig. 3 illustrates the constraints of *ShapeFit* parameters from three different tracers. On the top left is LRG, the top right is ELG, and the bottom is QSO. Similar to Fig. 2, PYBIRD can produce unbiased constraints on the *ShapeFit* parameters.

Fig. 2 and Fig. 3 illustrate that *Full-Modelling* and *Shapefit* with PYBIRD can return unbiased constraints. Fig. 4 compares the constraints of cosmological parameters from *ShapeFit* and *Full-Modelling*. The constraints of all cosmological parameters are within  $1\sigma$  of their

	BOSS MaxF	BOSS MinF	MaxF	MinF
$b_1$	$\mathcal{U}[0.0, 4.0]$	$\mathcal{U}[0.0, 4.0]$	$\mathcal{U}[0.0, 4.0]$	$\mathcal{U}[0.0, 4.0]$
$b_2$	$\mathcal{U}[-15.0, 15.0]$	1.0	$\mathcal{U}[-15.0, 15.0]$	1.0
$b_3$	$\mathcal{N}[0, 2]$	$\frac{294-1015(b_1-1)}{441}$	$\mathcal{N}[0, 10]$	$\frac{294-1015(b_1-1)}{441}$
$b_4$	$b_2$	$\mathcal{U}[-15.0, 15.0]$	$\mathcal{U}[-15.0, 15.0]$	$\mathcal{U}[-15.0, 15.0]$
$c_{ct}$	$\mathcal{N}[0, 2]$	$\mathcal{N}[0, 2]$	$\mathcal{U}[-\infty, \infty]$	$\mathcal{U}[-\infty, \infty]$
$c_{r,1}$	$\mathcal{N}[0, 8]$	$\mathcal{N}[0, 8]$	$\mathcal{U}[-\infty, \infty]$	$\mathcal{U}[-\infty, \infty]$
$c_{r,2}$	0	0	0	0
$c_{\epsilon,1}/\overline{n_g}$	$\mathcal{N}[0, 800]$	$\mathcal{N}[0, 800]$	$\mathcal{U}[-\infty, \infty]$	$\mathcal{U}[-\infty, \infty]$
$c_{\epsilon,2}/\overline{n_g}$	$\mathcal{N}[0, \frac{20000}{3}]$	0	0	0
$c_{\epsilon,3}/\overline{n_g}$	$\mathcal{N}[0, \frac{20000}{3}]$	$\mathcal{N}[0, \frac{20000}{3}]$	$\mathcal{U}[-\infty, \infty]$	$\mathcal{U}[-\infty, \infty]$

**Table 2.** The priors on the bias, counter, and stochastic terms for different prior configurations when fitting only the **monopole and quadrupole**. In this paper, we will mainly use the “BOSS MaxF” and “BOSS MinF” configurations. The “MaxF” and “MinF” configurations are used in the comparison paper in order to compare with other pipelines in DESI. For both “BOSS MinF” and “MinF” configurations, the values for  $b_2, b_3$ , and  $b_4$  are determined by the local Lagrangian approximation. The derivation is shown in the Appendix A. When we also fit the **hexadecapole**, for “BOSS MaxF” and “BOSS MinF” configurations, we follow [15] to change  $c_{r,1}$  prior to  $\mathcal{N}[0, 4]$  and put a  $\mathcal{N}[0, 4]$  prior on  $c_{r,2}$ . For the “MaxF” and “MinF” configurations, we impose an infinite flat prior on  $c_{r,2}$ .

respective truth values, albeit  $\Omega_{\text{cdm}}h^2$  is slightly more biased than the others. Generally, they are in good agreement with each other. There is around  $0.3\sigma$  shift in  $\ln(10^{10}A_s)$ , which leads to the small difference between *Shapefit* and *Full-Modelling* best-fit in Fig. 1. However, the difference in best-fit in Fig. 1 is less than  $0.3\sigma$ , this implies the difference in  $\ln(10^{10}A_s)$  could be absorbed by the nuisance parameters. Additionally, *Shapefit* and *Full-Modelling* may weigh the data in different ways, such as *Shapefit* does not care about the BAO relative amplitude. This could also contribute to the difference in the  $\ln(10^{10}A_s)$  constraints. Furthermore, the degeneracies between the nuisance parameters and the cosmological/*Shapefit* parameters are also different. This could also shift the constraints on the cosmological parameters. However, the shift here is small compared to the constraints of the cosmological parameters, so we expect it to have only a small impact on the constraints from DESI.

In summary, we find that PYBIRD can give unbiased constraints of cosmological parameters for the  $\Lambda$ CDM model with  $k_{\text{max}} = 0.20h\text{Mpc}^{-1}$ , without the hexadecapole, and with the “BOSS MaxF” configurations for the  $\Lambda$ CDM model for both *Shapefit* and *Full-Modelling* approaches. In section 5 and 6, we extend these analyses for the  $w$ CDM and the  $o$ CDM model. We find that these extended cosmological models, including the hexadecapole and change to the “BOSS MinF” will significantly improve the constraints. Furthermore, the constraints from *ShapeFit* and *Full-Modelling* are in excellent agreement, and the systematic shift in  $\ln(10^{10}A_s)$  is small. In the remainder of this work, we will show that the accuracy of PYBIRD remains good even for reasonable extension beyond this configuration, including extended cosmological models.

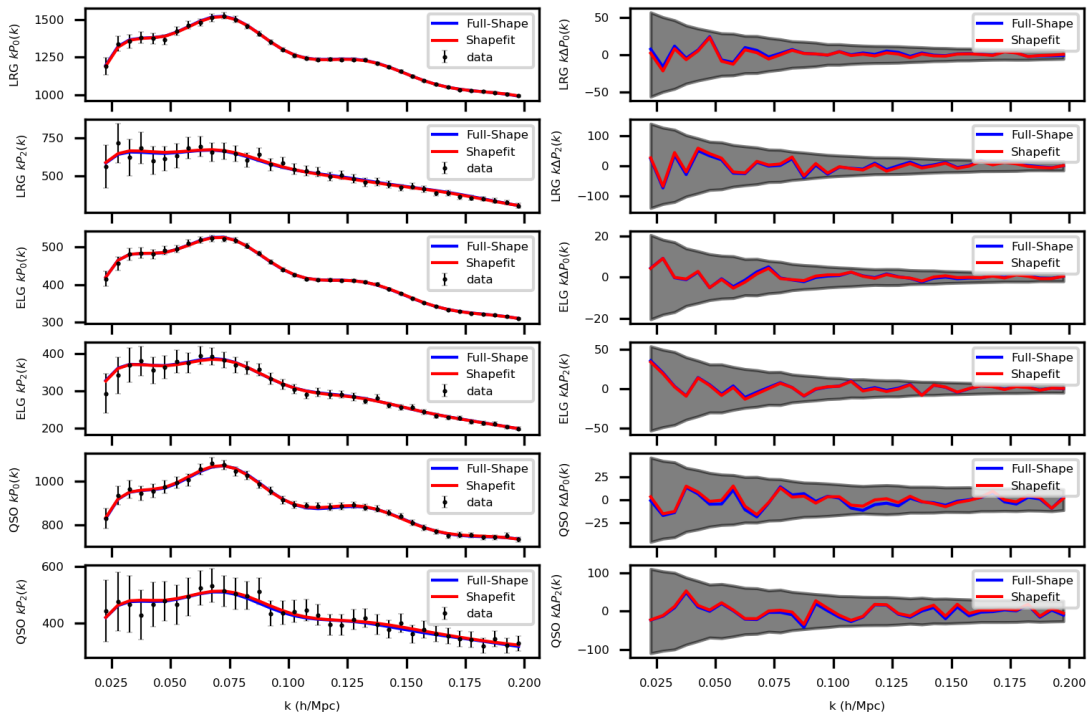


**Figure 1.** This plot shows the best-fit model of the power spectrum from the LRG, ELG, and QSO mocks for both *Full-Modelling* and *ShapeFit* methods. We use  $k_{\max} = 0.20h\text{Mpc}^{-1}$ , “BOSS MaxF” prior, and without the hexadecapole to generate this plot. On the left, the error bar is given by the single box covariance matrix, which indicates the statistical error from the DESI Y5 survey. On the right, the shaded area is the data power spectrum uncertainty, and the lines are the difference between the best-fit power spectrum and the data power spectrum. The best-fit power spectrum from both *ShapeFit* and *Full-Modelling* are in good agreement with each other. The maximum deviation between the two is from the QSO because the power spectrum from QSO has a larger error, which gives these two models more freedom. Lastly, the plot also shows the best-fit models from both methods are well within the uncertainty of the measurement indicating our model is a good fit for the data.

## 5 *ShapeFit* tests

In this section, we test the impact of fitting up to different  $k_{\max}$  scales, including the hexadecapole, and different configurations for priors using the *ShapeFit* method.

### 5.1 Effect of $k_{\max}$

Fig. 5 illustrates how the constraints on the *ShapeFit* parameters change with respect to  $k_{\max}$ . These plots are calculated with the single-box covariance matrix. You may notice that the constraints at  $k_{\max} = 0.20h\text{Mpc}^{-1}$  are slightly different from Fig 3. This is because to avoid cross-correlation between different redshift bins in the same realization when combining all redshift bins, we only use the mean of 8 different mocks for each tracer for Fig 3. However, we only focus on a single redshift bin for Fig. 5, so we use the mean of 25 different mocks to obtain more robust results. Increasing  $k_{\max}$  makes the constraints of the *ShapeFit* parameters tighter, but it also increases the systematic errors, particularly for the  $\alpha$  parameters. This is expected because, on one hand, increasing  $k_{\max}$  provides more information. On the other

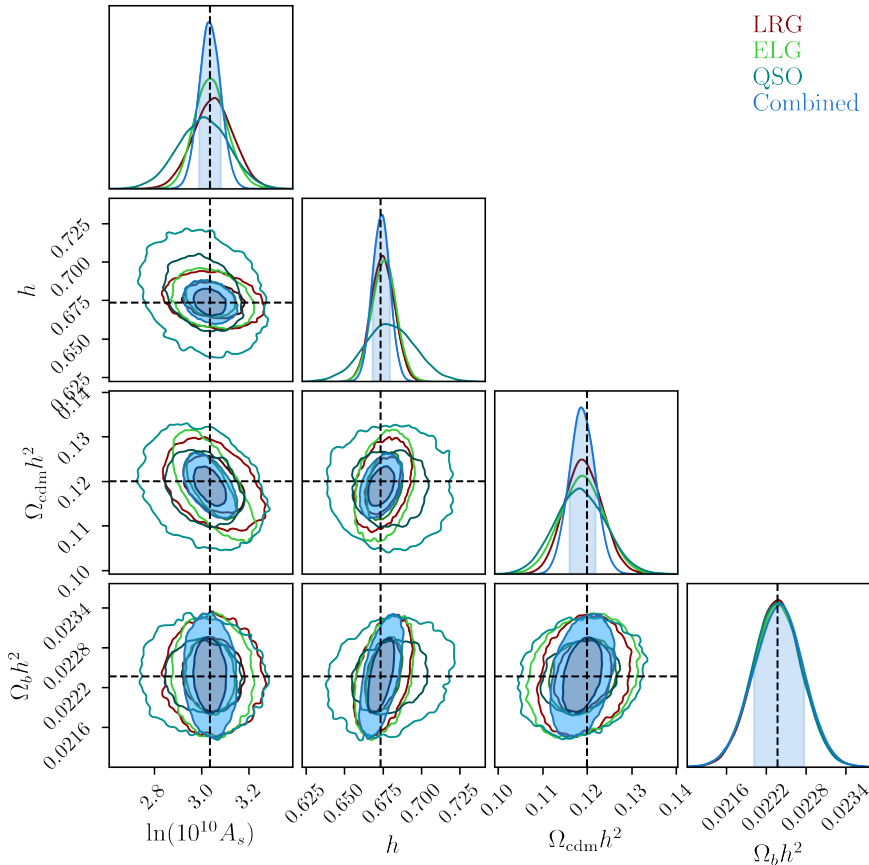


**Figure 2.** This plot illustrates the constraints on  $\Lambda$ CDM cosmological parameters using *Full-Modelling* with  $k_{\max} = 0.20h\text{Mpc}^{-1}$ , the “BOSS MaxF” prior, and without the hexadecapole using the LRG, ELG, and QSO mocks, and their combination. The dashed line indicates the truth values of the cosmological parameters. The constraints on  $\omega_b$  are dominated by the BBN prior. The QSO mock has weaker constraints than the other two tracers because it has a much lower number density. The combination of different tracers can significantly tighten the constraints on the cosmological parameters. Furthermore, PYBIRD can produce unbiased constraints of the cosmological parameters in all cases.

hand, the EFT parameters become tightly anchored, and one is effectively only fitting a power law with little cosmological information. Table 3 compiles the constraints and the systematic error for the mean of the LRG, ELG, and QSO mocks with *ShapeFit*. Table 3 demonstrates the constraints on the  $\alpha$  parameters are similar for the LRG and ELG mocks but weaker for the QSO mocks because it has lower number density.

## 5.2 Including the hexadecapole

Fig. 6 illustrates the effect of adding hexadecapole on the constraints on cosmological parameters with the means of the LRG (left), ELG (right), and QSO (bottom) mocks. These constraints are calculated with the single-box covariance matrix. For all three tracers, the constraints for  $\alpha$  parameters are tightened significantly after including the hexadecapole. There are also small improvements for  $f\sigma_{88}$  but not  $m$  after adding the hexadecapole. This is likely because  $m$  is essentially a primordial factor contained in the underlying  $P_{\text{lin}}$ , whereas

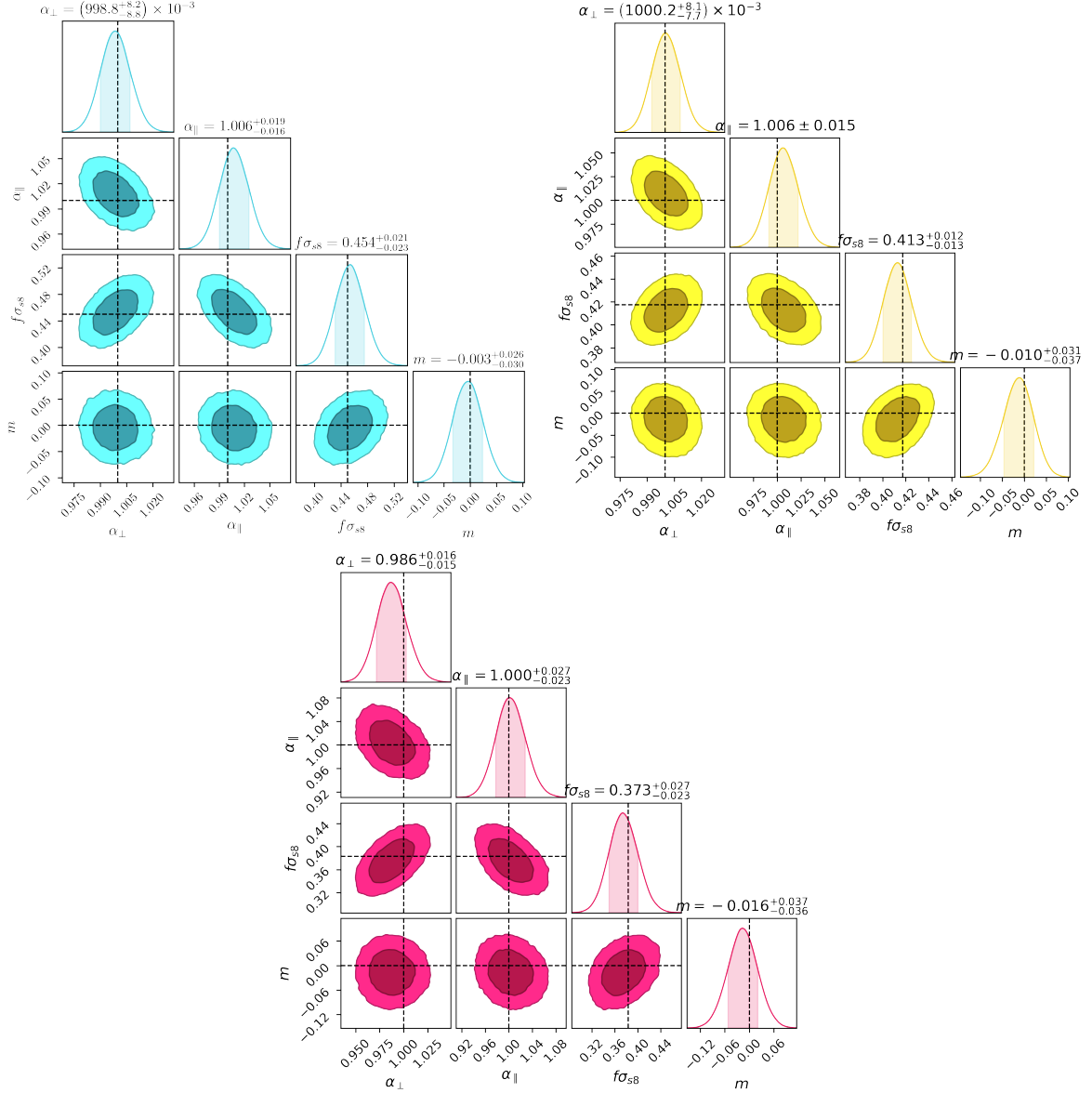


**Figure 3.** Constraints on the *ShapeFit* parameters from three different tracers with  $k_{\max} = 0.20h\text{Mpc}^{-1}$ , the “BOSS MaxF” prior, and without the hexadecapole. The top left is the constraints from LRG, the top right is from ELG, and the bottom is from QSO. Dashed lines correspond to the simulation expectations. Similar to the *Full-Modelling* constraints, PYBIRD can produce unbiased constraints on the *ShapeFit* parameters for all three tracers.

**Table 3.** A summary of the relative biases in the *ShapeFit* parameters with the single-box covariance matrix using the mean of LRG, ELG, and QSO mocks. The QSO mocks give much larger uncertainty because its number density is much lower than LRG and ELG, so the effective volume is smaller. Since the template cosmology is set to the true cosmology, the truth values are  $\alpha_{\perp} = \alpha_{\parallel} = r_A = 1.0$  and  $m = 0.0$ . The constraints on *ShapeFit* parameters become tighter when we use higher  $k_{\max}$  because they provide more information. However, the best-fits also deviate further from the truth value because the counter and stochastic terms dominate small-scale, so little cosmological information can be obtained. We found for  $k_{\max} = 0.20h\text{Mpc}^{-1}$ , the best-fit parameters are less than  $0.5\sigma$  from the best-fit. Therefore, we choose to use  $k_{\max} = 0.20h\text{Mpc}^{-1}$  for future fittings.

Tracer	$k_{\max}(h\text{Mpc}^{-1})$	$\Delta\alpha_{\perp}\%$	$\Delta\alpha_{\parallel}\%$	$\Delta r_A\%$	$m$
LRG	0.14	$-0.3^{+1.2}_{-1.3}$	$0.6^{+2.7}_{-2.3}$	$-0.4^{+6.5}_{-5.9}$	$-0.009^{+0.031}_{-0.038}$
LRG	0.16	$-0.28^{+1.16}_{-0.98}$	$0.0^{+2.3}_{-2.1}$	$1.0^{+6.1}_{-5.1}$	$-0.011^{+0.034}_{-0.031}$
LRG	0.18	$-0.32^{+0.93}_{-0.94}$	$0.6^{+2.0}_{-1.8}$	$-0.2^{+5.6}_{-4.5}$	$-0.014^{+0.030}_{-0.031}$
LRG	0.20	$-0.38^{+0.85}_{-0.86}$	$0.8^{+1.7}_{-1.8}$	$0.1^{+4.9}_{-4.7}$	$-0.012^{+0.032}_{-0.026}$
LRG	0.22	$-0.37^{+0.71}_{-0.79}$	$1.0^{+1.5}_{-1.7}$	$0.8^{+4.9}_{-4.4}$	$-0.005^{+0.024}_{-0.031}$
LRG	0.24	$-0.47^{+0.69}_{-0.75}$	$1.3^{+1.5}_{-1.9}$	$1.2 \pm 4.6$	$-0.002^{+0.026}_{-0.025}$
LRG	0.26	$-0.47^{+0.63}_{-0.78}$	$1.4^{+1.7}_{-1.5}$	$1.9^{+4.7}_{-4.3}$	$0.001^{+0.026}_{-0.024}$
LRG	0.28	$-0.80^{+0.66}_{-0.70}$	$2.2 \pm 1.6$	$1.8^{+4.4}_{-4.5}$	$0.003^{+0.023}_{-0.026}$
ELG	0.14	$-0.5^{+1.5}_{-1.1}$	$0.7^{+2.6}_{-2.1}$	$-0.8^{+4.2}_{-4.3}$	$-0.014^{+0.041}_{-0.039}$
ELG	0.16	$-0.24^{+1.13}_{-0.96}$	$0.5^{+1.9}_{-2.1}$	$0.0^{+4.0}_{-4.3}$	$-0.013^{+0.033}_{-0.042}$
ELG	0.18	$-0.26^{+0.91}_{-0.86}$	$0.2^{+1.8}_{-1.7}$	$-1.1^{+3.9}_{-2.7}$	$-0.010^{+0.029}_{-0.037}$
ELG	0.20	$-0.41^{+0.83}_{-0.75}$	$0.3^{+1.9}_{-1.3}$	$-0.2^{+3.4}_{-3.0}$	$-0.018^{+0.037}_{-0.029}$
ELG	0.22	$-0.31^{+0.63}_{-0.73}$	$0.9^{+1.3}_{-1.5}$	$-0.1^{+3.3}_{-3.0}$	$-0.015^{+0.037}_{-0.027}$
ELG	0.24	$-0.39^{+0.65}_{-0.63}$	$0.7^{+1.4}_{-1.3}$	$0.3^{+3.1}_{-2.9}$	$-0.001^{+0.027}_{-0.033}$
ELG	0.26	$-0.41^{+0.62}_{-0.64}$	$1.0 \pm 1.4$	$0.7 \pm 2.9$	$-0.002^{+0.027}_{-0.030}$
ELG	0.28	$-0.64^{+0.64}_{-0.51}$	$1.0^{+1.5}_{-1.2}$	$1.1^{+2.5}_{-3.0}$	$0.003^{+0.023}_{-0.033}$
QSO	0.14	$-0.5^{+2.0}_{-2.3}$	$0.4^{+3.6}_{-3.1}$	$-2.3^{+8.5}_{-7.6}$	$-0.013^{+0.037}_{-0.047}$
QSO	0.16	$-0.7^{+2.2}_{-1.7}$	$0.0^{+3.3}_{-2.8}$	$-1.8^{+8.2}_{-6.0}$	$-0.018^{+0.041}_{-0.037}$
QSO	0.18	$-0.6^{+1.7}_{-1.6}$	$0.7^{+2.6}_{-2.9}$	$-0.7^{+6.4}_{-6.8}$	$-0.015^{+0.035}_{-0.041}$
QSO	0.20	$-0.2^{+1.3}_{-1.9}$	$0.2^{+3.1}_{-2.1}$	$-1.6^{+6.8}_{-6.0}$	$-0.013^{+0.036}_{-0.037}$
QSO	0.22	$-0.6^{+1.5}_{-1.4}$	$0.4^{+2.8}_{-2.1}$	$-1.4^{+6.4}_{-6.2}$	$-0.010^{+0.031}_{-0.039}$
QSO	0.24	$-0.5^{+1.3}_{-1.5}$	$0.5^{+2.7}_{-2.2}$	$-0.6^{+6.1}_{-6.3}$	$-0.018^{+0.036}_{-0.030}$
QSO	0.26	$-0.5^{+1.3}_{-1.6}$	$0.6^{+2.5}_{-2.3}$	$-0.1^{+5.6}_{-6.5}$	$-0.008^{+0.027}_{-0.035}$
QSO	0.28	$-0.6^{+1.3}_{-1.4}$	$1.1^{+2.3}_{-2.6}$	$-0.6 \pm 5.9$	$-0.009^{+0.029}_{-0.031}$



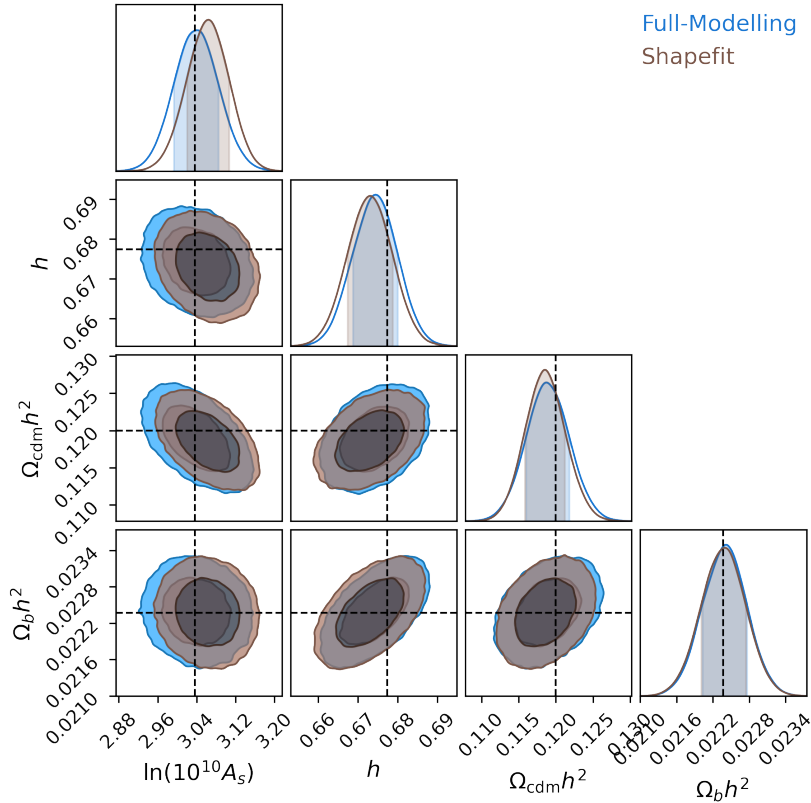


**Figure 4.** This plot compares the constraints of cosmological parameters using all tracers from *ShapeFit* and *Full-Modelling* with  $k_{\max} = 0.20h\text{Mpc}^{-1}$ , the “BOSS MaxF” prior, and without the hexadecapole. The constraints are in good agreement with each other. Nonetheless, the shift in  $\ln(10^{10}A_s)$  is around than  $0.3\sigma$ , so the systematic shift will not dominate the error bar.

the hexadecapole mainly contains the late-time RSD effects. Hence, from a physical point of view, it makes sense that the hexadecapole (and even the quadrupole) contain very little information on  $m$ . The constraints of *ShapeFit* parameters are still consistent with the truth value after adding the hexadecapoles.

### 5.3 Maximum and minimum freedom

Fig. 7 shows the constraints on the *ShapeFit* parameters after fixing  $b_2$  and  $b_3$  based on the local Lagrangian relation and  $c_{\epsilon,2}$  to zero (“BOSS MinF” configuration). We choose to fix  $c_{\epsilon,2}$  to zero to compare with other pipelines in DESI since the other models do not include a term with similar proportionality by default. We find that fixing these parameters tightens the constraint on  $m$ , and the final constraints after fixing these parameters are still consistent with the truth values. The improvement in  $m$  mainly arises because of the degeneracy between  $m$  and  $b_3$  when the latter is allowed to be free.

## 6 *Full-Modelling* tests

Similar to Section 5, we now test the same configurations for the *Full-Modelling* fit. Furthermore, we also compare the constraints from *ShapeFit* and *Full-Modelling* fit with different cosmological models.

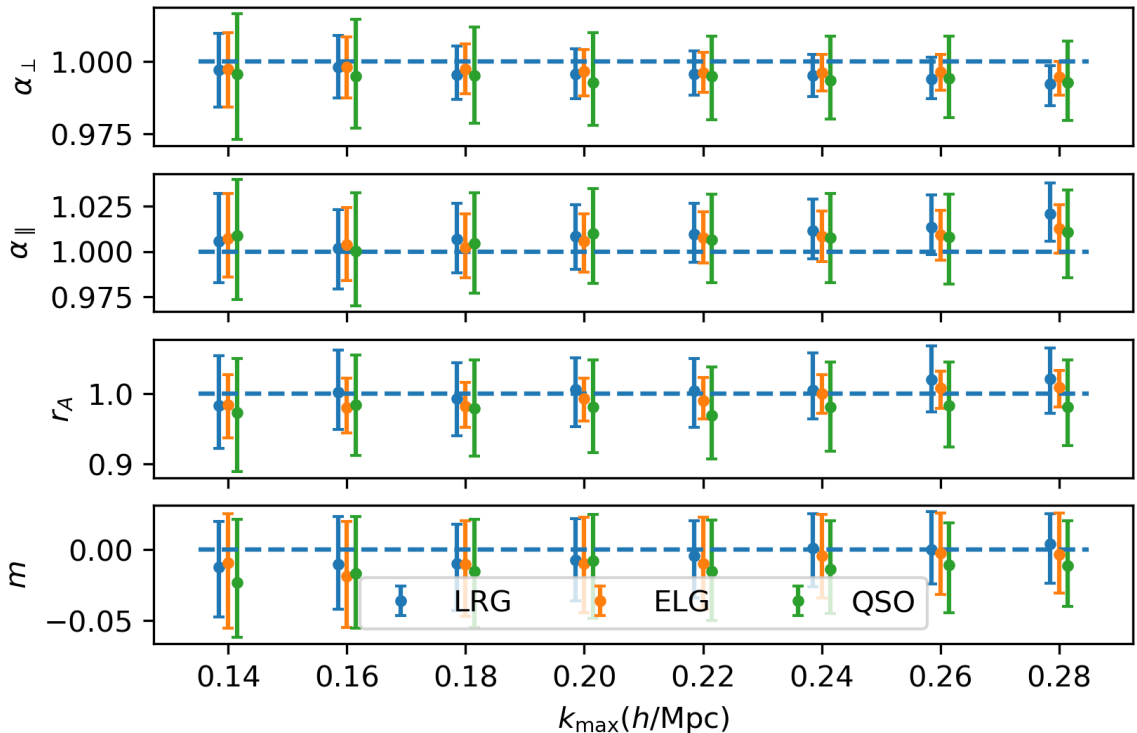


**Figure 5.** Constraints on the *ShapeFit* parameters with different  $k_{\max}$  from the mean of the LRG mocks (blue), ELG mocks (orange), and the QSO mocks (green) with the “BOSS MaxF” prior and without the hexadecapole. The template parameters are fixed to the true cosmology. PYBIRD can produced unbiased constraints on the *ShapeFit* parameters for all three tracers up to  $k_{\max} = 0.26 h\text{Mpc}^{-1}$ . However, the systematic errors for the Shapfit parameters are bigger than  $0.5\sigma$  if  $k_{\max} > 0.20 h\text{Mpc}^{-1}$ . Therefore, we decide to use  $k_{\max} = 0.20 h\text{Mpc}^{-1}$  for future analysis.

### 6.1 Effect of $k_{\max}$

Fig. 8 shows the constraints from *Full-Modelling* fitting with the mean of the mocks with different choices of  $k_{\max}$ . Similar to the *ShapeFit* results, increasing  $k_{\max}$  will increase the constraining power but also increase the systematic bias. The constraints on cosmological parameters from different tracers are consistent with each other. QSO mocks give larger errors similar to *ShapeFit* because its number density is lower. There is a trend that the best-fit  $\ln(10^{10} A_s)$  increases as  $k_{\max}$  increases. This only occurs beyond  $k_{\max} = 0.22 h\text{Mpc}^{-1}$ , where the small-scale systematics begins to creep in. For consistency, we also choose to fix  $k_{\max} = 0.20 h\text{Mpc}^{-1}$  for future analysis, the same as *ShapeFit*. A summary of the parameter biases is presented in Table 4.

Using our preferred value of  $k_{\max} = 0.20 h\text{Mpc}^{-1}$ , Fig. 9 illustrates the constraints on cosmological parameters in the  $w\text{CDM}$  (left) and  $o\text{CDM}$  models (right) with the combination of LRG, ELG, and QSO mocks. The corresponding plot for  $\Lambda\text{CDM}$  was shown earlier in Fig. 2. Switching from  $\Lambda\text{CDM}$  to  $w\text{CDM}$  or  $o\text{CDM}$  significantly weakens the constraints on the base  $\Lambda\text{CDM}$  parameters. In the case of  $w\text{CDM}$  and  $o\text{CDM}$ ,  $\ln(10^{10} A_s)$  and  $h$  are weakened compared to Fig. 2 because they are both degenerate with the dark energy equation of state  $w$  and curvature  $\Omega_k$ . For  $w\text{CDM}$ , this also shifts  $h$  to a higher value and  $\ln(10^{10} A_s)$  to a lower value. However, the error bars on these parameters are large enough in both

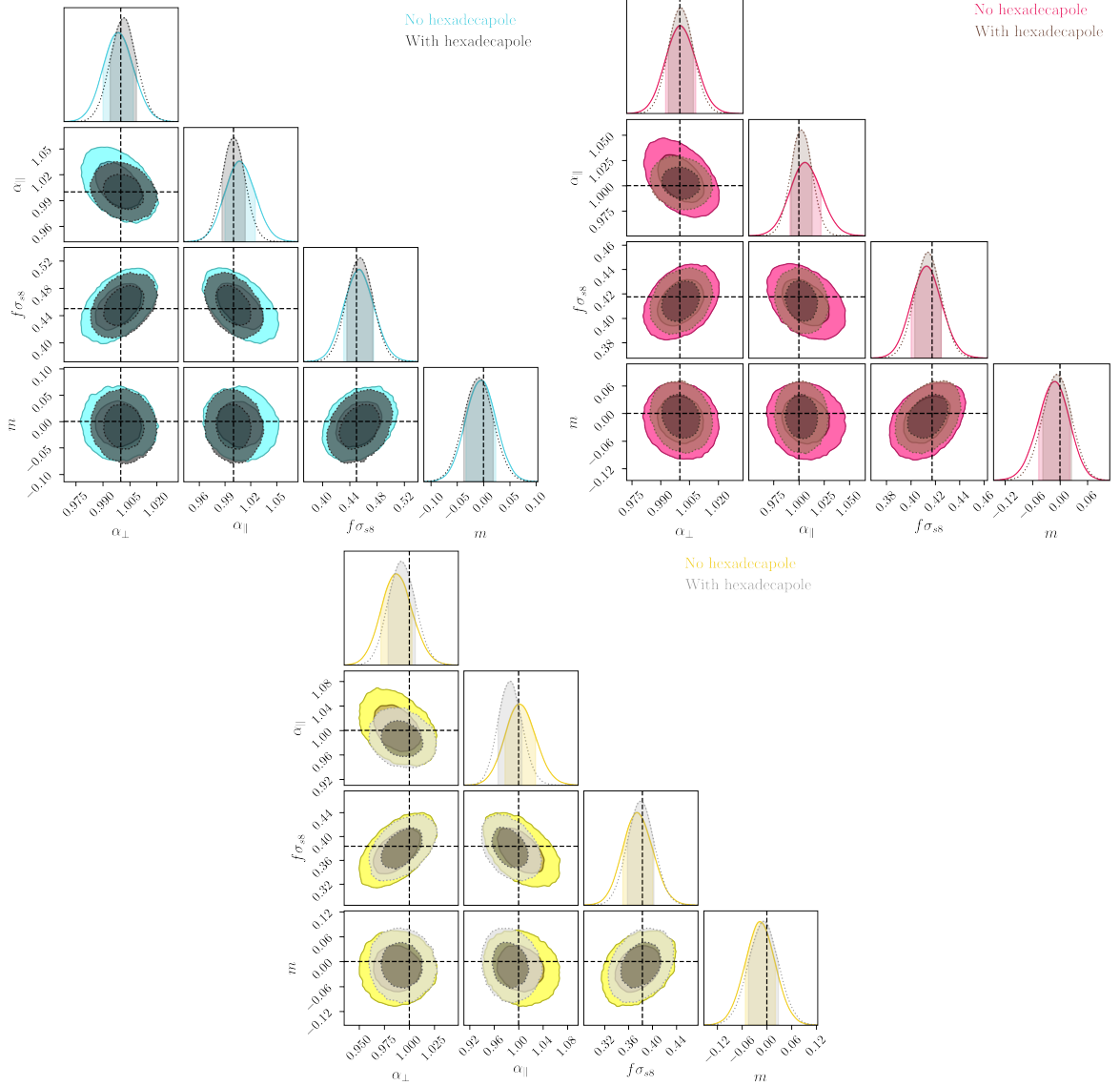


**Figure 6.** Comparing constraints on the *ShapeFit* parameters with  $k_{\max} = 0.20 h\text{Mpc}^{-1}$  with or without the hexadecapole using the LRG mocks (top left), ELG mocks (top right), and QSO mocks (bottom) with “BOSS MaxF” prior. These plots demonstrate that including the hexadecapole can significantly tighten the constraints for the  $\alpha$  parameters and drive them closer to the truth value. Including the hexadecapole can also slightly tighten the constraints for  $f\sigma_{88}$ . Overall, the constraints of *ShapeFit* parameters after including the hexadecapole show no substantial biases for this choice of  $k_{\max}$ .

**Table 4.** This table shows the constraints on the cosmological parameters in the  $\Lambda$ CDM model with the *Full-Modelling* fit using the single-box covariance matrix. Similar to *ShapeFit*, the constraints on cosmological parameters increase when we use higher  $k_{\max}$  because it contains more information. However, it will increase the systematic error because our model fails to model the small-scale power spectrum. We choose to fit with  $k_{\max} = 0.20h\text{Mpc}^{-1}$  for later tests because it provides one of the tightest constraints and with systematic error less than  $0.5\sigma$ .

Tracer	$k_{\max}(\text{Mpc}^{-1})$	$\Delta \ln(10^{10} A_s)\%$	$\Delta h\%$	$\Delta \Omega_{\text{cdm}} h^2\%$	$\Delta \Omega_b h^2\%$
LRG	0.14	$0.7^{+3.0}_{-3.3}$	$0.2^{+1.5}_{-1.7}$	$-1.5^{+4.8}_{-3.7}$	$0.1^{+1.5}_{-1.8}$
LRG	0.16	$0.7^{+2.9}_{-3.3}$	$0.4^{+1.3}_{-1.4}$	$-0.5^{+4.1}_{-4.2}$	$0.1^{+1.7}_{-1.6}$
LRG	0.18	$0.5^{+2.9}_{-3.1}$	$0.1^{+1.3}_{-1.0}$	$-0.9 \pm 3.8$	$0.0^{+1.6}_{-1.7}$
LRG	0.20	$0.7^{+2.6}_{-3.0}$	$0.2^{+1.1}_{-1.2}$	$-1.0^{+3.7}_{-3.3}$	$0.1^{+1.6}_{-1.7}$
LRG	0.22	$0.9^{+2.7}_{-2.3}$	$0.02^{+1.22}_{-0.88}$	$-0.4^{+3.1}_{-3.8}$	$0.1^{+1.6}_{-1.8}$
LRG	0.24	$1.7^{+2.7}_{-2.2}$	$0.3^{+1.1}_{-1.0}$	$-0.2^{+3.2}_{-3.4}$	$0.1^{+1.6}_{-1.7}$
LRG	0.26	$3.2^{+2.1}_{-2.5}$	$0.2^{+1.1}_{-1.0}$	$-0.5^{+3.5}_{-3.3}$	$-0.1^{+1.7}_{-1.6}$
LRG	0.28	$4.6^{+1.8}_{-2.6}$	$0.1^{+1.3}_{-1.0}$	$-1.4^{+4.4}_{-2.7}$	$0.1^{+1.6}_{-1.8}$
ELG	0.14	$-0.1^{+2.6}_{-3.3}$	$0.2^{+1.8}_{-1.7}$	$0.2^{+5.3}_{-6.2}$	$0.0 \pm 1.7$
ELG	0.16	$0.0^{+2.3}_{-3.2}$	$0.3^{+1.6}_{-1.4}$	$-0.8^{+4.8}_{-5.3}$	$0.1^{+1.6}_{-1.8}$
ELG	0.18	$-0.3^{+2.3}_{-2.6}$	$0.3^{+1.3}_{-1.2}$	$-0.9^{+4.5}_{-4.3}$	$-0.2^{+1.8}_{-1.5}$
ELG	0.20	$-0.1 \pm 2.3$	$0.3^{+1.2}_{-1.1}$	$-1.2^{+4.4}_{-3.9}$	$0.1 \pm 1.7$
ELG	0.22	$0.1^{+2.3}_{-2.0}$	$0.3^{+1.1}_{-1.0}$	$-0.7^{+4.0}_{-4.3}$	$-0.1^{+1.7}_{-1.6}$
ELG	0.24	$0.3^{+2.2}_{-1.8}$	$0.23^{+1.02}_{-0.96}$	$0.3^{+3.4}_{-4.4}$	$0.2^{+1.4}_{-1.9}$
ELG	0.26	$0.7^{+2.1}_{-1.6}$	$0.44^{+0.85}_{-1.15}$	$0.1^{+3.6}_{-4.0}$	$-0.1^{+1.7}_{-1.6}$
ELG	0.28	$1.0^{+2.0}_{-1.6}$	$0.49^{+0.91}_{-1.09}$	$1.2^{+3.2}_{-4.7}$	$-0.1 \pm 1.7$
QSO	0.14	$-0.5^{+3.5}_{-4.4}$	$0.9^{+3.7}_{-2.8}$	$-2.2^{+5.7}_{-4.9}$	$-0.1^{+1.6}_{-1.7}$
QSO	0.16	$-1.7^{+4.6}_{-2.9}$	$0.7^{+3.4}_{-2.3}$	$-1.8^{+5.8}_{-4.5}$	$0.0^{+1.7}_{-1.6}$
QSO	0.18	$-1.4^{+4.2}_{-3.2}$	$1.3^{+2.2}_{-2.8}$	$-2.2^{+5.3}_{-4.4}$	$-0.1 \pm 1.7$
QSO	0.20	$-0.9^{+3.6}_{-3.5}$	$0.3^{+2.9}_{-2.0}$	$-1.3^{+4.7}_{-4.8}$	$0.0^{+1.5}_{-1.7}$
QSO	0.22	$-0.7 \pm 3.4$	$0.8^{+2.5}_{-2.0}$	$-2.3^{+5.4}_{-3.7}$	$0.2^{+1.5}_{-1.8}$
QSO	0.24	$-0.6^{+3.5}_{-3.0}$	$0.9^{+2.2}_{-2.3}$	$-1.6^{+4.6}_{-4.1}$	$0.2^{+1.5}_{-1.9}$
QSO	0.26	$-0.3^{+3.3}_{-2.8}$	$1.3^{+1.9}_{-2.5}$	$-1.7^{+4.7}_{-3.6}$	$0.0^{+1.7}_{-1.6}$
QSO	0.28	$0.0^{+3.3}_{-2.6}$	$1.0^{+2.1}_{-2.3}$	$-1.5^{+4.7}_{-3.5}$	$0.1^{+1.6}_{-1.7}$

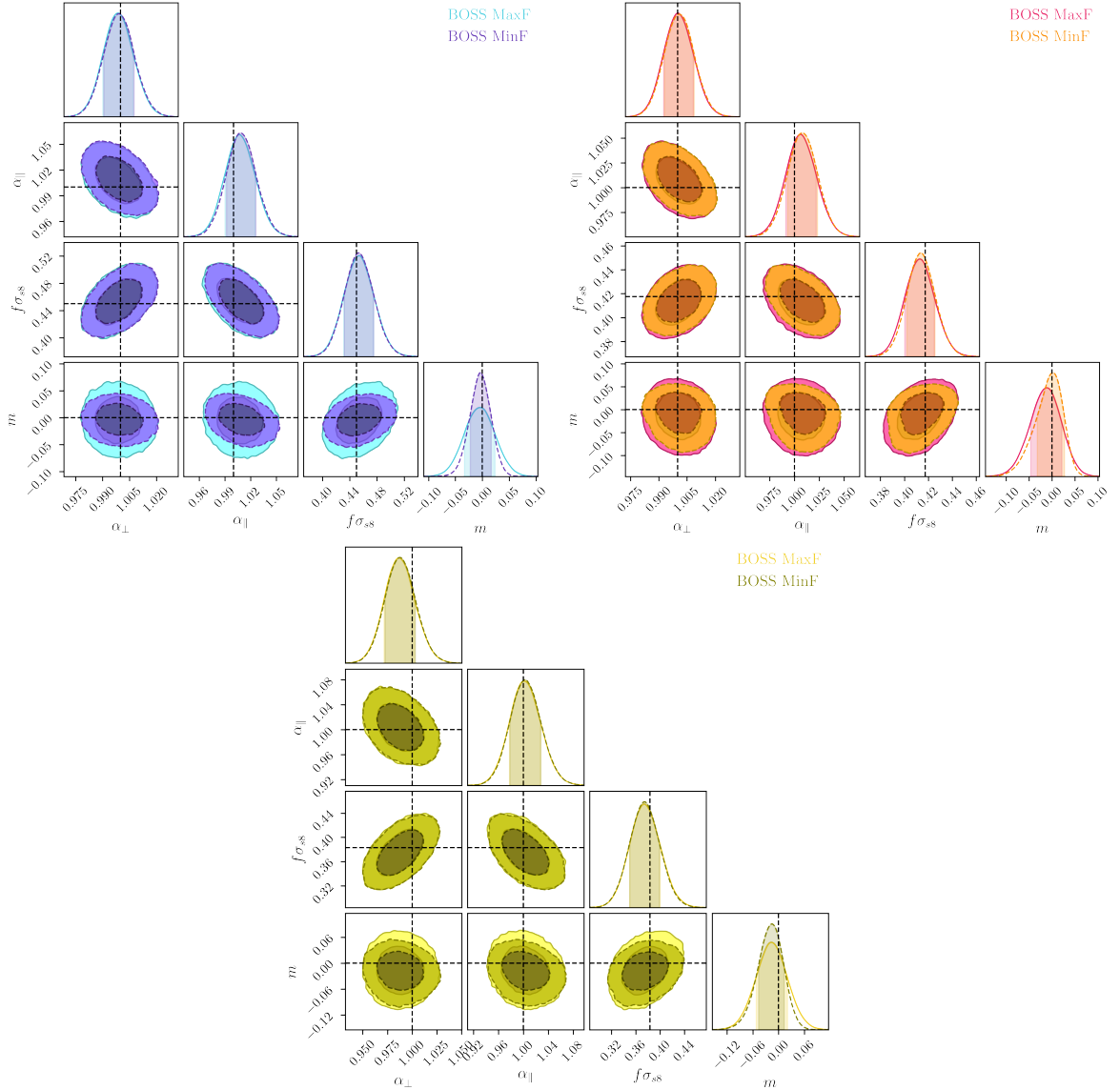


**Figure 7.** The effect of changing the prior configurations from “BOSS MaxF” to “BOSS MinF” for LRG (top left), ELG (top right), and QSO (bottom) with  $k_{\max} = 0.20h^{-1}\text{Mpc}$ . Changing the prior configuration provides a much tighter constraint on  $m$ . This is because  $b_3$  is degenerate with  $m$ , which is fixed in the “BOSS MinF” configuration.

extended models that they remain consistent with the truth values within the  $1\sigma$  level.

## 6.2 Including the hexadecapole

Fig. 10 illustrates the constraints on cosmological parameters after adding the hexadecapole for the combination of the LRG, ELG, and QSO mocks. In general, adding the hexadecapole has little impact in the  $\Lambda\text{CDM}$  model. This is contrary to the results from *ShapeFit* (Fig. 6) where we see improved constraints on all *ShapeFit* parameters. We find this is due to the internal prior of  $\Lambda\text{CDM}$  on the *ShapeFit* parameters, which allows for little additional information to be gleaned from this low amplitude multipole.

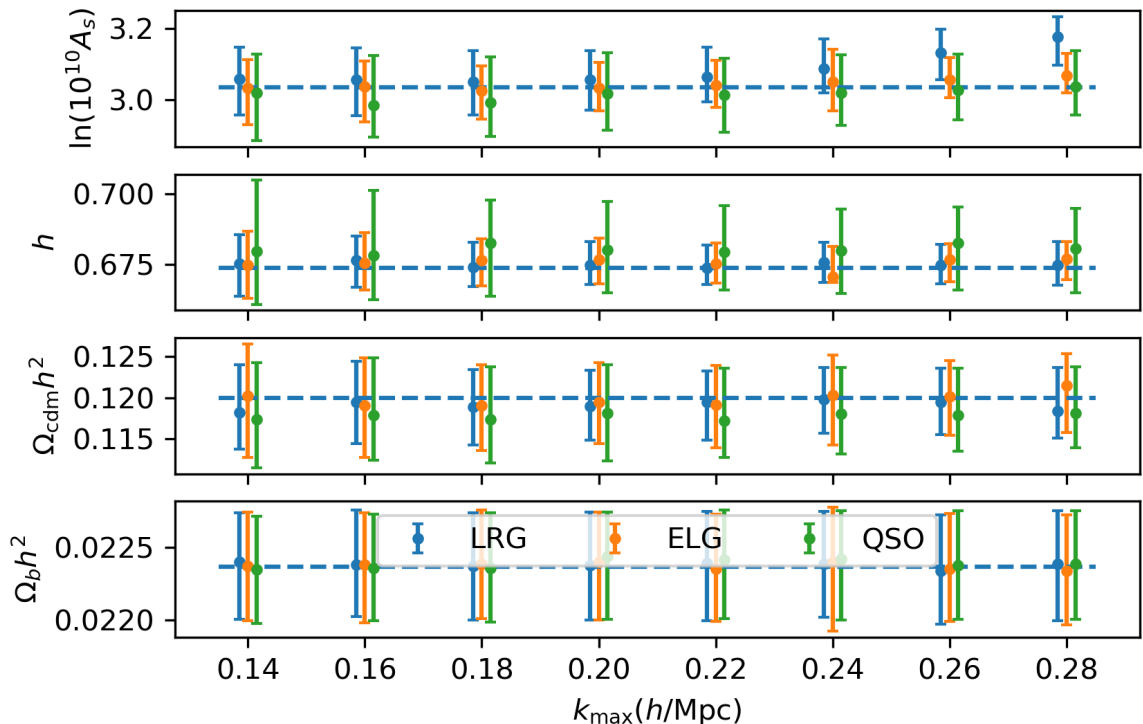


**Figure 8.** The constraints of cosmological parameters with the mean of the LRG mocks (blue), ELG mocks (orange), and QSO mocks (green) using the *Full-Modelling* fit with the “BOSS MaxF” prior. The dashed lines are the truth values. For  $\Omega_b h^2$ , the constraints are dominated by its Gaussian prior. The best-fits of  $\ln(10^{10} A_s)$  increases as the  $k_{\max}$  increases. This is expected since the systematic error increases at larger  $k_{\max}$  because our model fails to model the small-scale.

However, for other cosmological models, this is not the case. The constraints for  $h$  and  $w$  are tighter and closer to the truth value after including the hexadecapole. It also shifts  $\ln(10^{10} A_s)$  slightly because it is highly degenerate with  $h$  and  $w$ . Similarly, adding the hexadecapole when fitting the  $\Lambda$ CDM model also significantly improves the constraints for  $\ln(10^{10} A_s)$ ,  $h$ , and  $\Omega_k$ . In both cases, adding the hexadecapole reduces the systematic bias for  $k_{\max} = 0.20 h \text{Mpc}^{-1}$ . Therefore, we recommend including it in cosmological analyses for extended cosmological models.

### 6.3 Maximum and minimum freedom

Fig. 11 demonstrates the effect of fixing  $b_2$  and  $b_3$  to the local Lagrangian relation, and  $c_{\epsilon,2}$  to zero for the *Full-Modelling* fit with the combination of the LRG, ELG, and QSO mocks. Fixing these parameters provides a tighter constraint for  $\Omega_{\text{cdm}} h^2$ . This is consistent with the results from *ShapeFit* where the constraint on  $m$  is tighter with the “BOSS MinF” configuration. This effect also holds for the cases of  $w$ CDM and  $\Lambda$ CDM. However, the constraints on the extended cosmological parameters  $w$  and  $\Omega_k$  themselves are largely unaffected, as these primarily change the overall amplitude of the power spectrum and the redshift-distance relationship, rather than the power spectrum tilt.<sup>4</sup> All cosmological parameters remain consistent

<sup>4</sup>Note that this is true for the smooth ‘background’ form of dark energy tested here, wherein forms of Dark Energy with  $w < -1$  are in any case somewhat unphysical as they result in an unstable vacuum energy density.

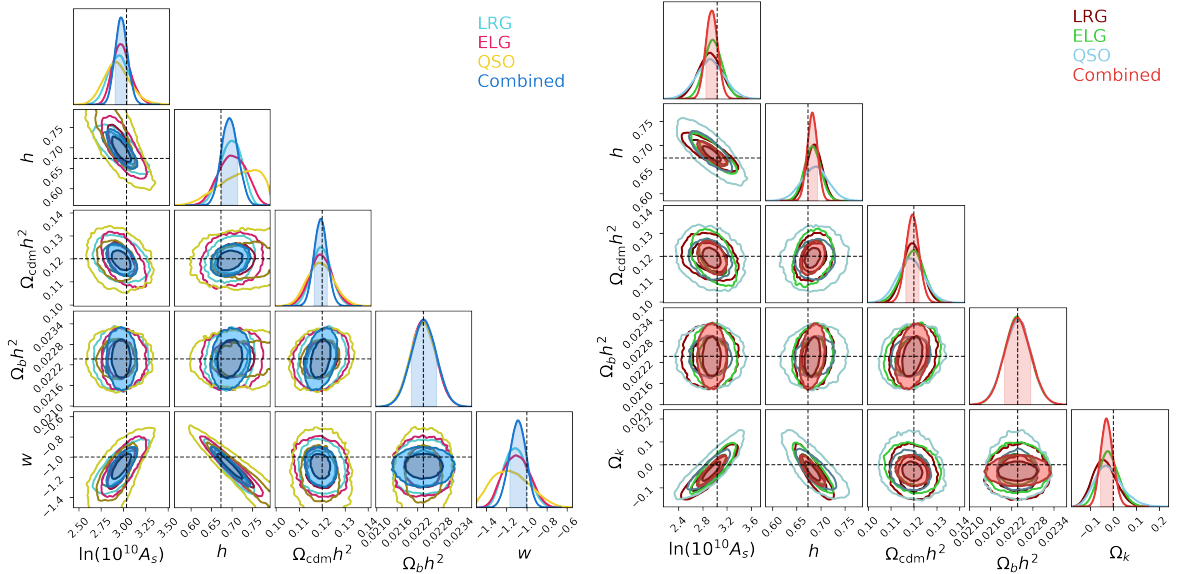


**Figure 9.** Constraints on the cosmological parameters in the  $w$ CDM (left) and  $o$ CDM (right) models with different tracers using the *Full-Modelling* fitting methodology with the “BOSS MaxF” prior and  $k_{\max} = 0.20h/\text{Mpc}$ . Similar to Fig. 2, adding different tracers together significantly improves the constraints on the cosmological parameters. All the constraints are still consistent with the truth value within  $1\sigma$ , but we see larger deviations from the truth for  $\ln(10^{10}A_s)$  and  $h$ . This is because these two parameters are highly degenerate with  $w$  and  $\Omega_k$ , which moves them further away from the truth in the marginalized one-dimensional posterior. However, since these parameters are highly degenerate with each other, the two-dimensional contour demonstrates that the constraints are still within  $1\sigma$ .

with their respective truth values with the “BOSS MinF” configuration.

#### 6.4 Comparing *ShapeFit* vs *Full-Modelling*

Having investigated how different analysis choices affect both the *ShapeFit* and *Full-Modelling* fitting methodologies, we now try to validate the two methods to give consistent results for the extended cosmology. The case for  $\Lambda$ CDM was presented in Fig. 4, now Fig. 12 illustrates that the constraints on cosmological parameters in both  $w$ CDM and  $o$ CDM cosmologies from *Full-Modelling* and *ShapeFit* are also mostly consistent with each other except for small shifts in  $w$  (for  $w$ CDM,  $\Omega_k$  for  $o$ CDM),  $\ln(10^{10}A_s)$  and  $h$  parameters. These shifts are similar to the shift seen in  $\ln(10^{10}A_s)$  for the case of  $\Lambda$ CDM, propagating along the degeneracy between  $\ln(10^{10}A_s)$ ,  $h$  and the extended cosmological parameters.

### 7 Correlation function

Having fully validated and explored different modeling choices when applying the PYBIRD algorithm to our mock power spectrum measurements, we now demonstrate that these results also apply to the case of a correlation function analysis. In PYBIRD, this is done by computing

---

However, in the case of ‘clustering’ quintessence models that allow for a physical mechanism in which solutions with  $w < -1$  can arise, the clustering of the Dark Energy fluid itself can give rise to scale-dependent effects that could change the tilt of the power spectrum. In that case, improved constraints on the  $m$  parameter could result in improved constraints on the parameters of Dark Energy.

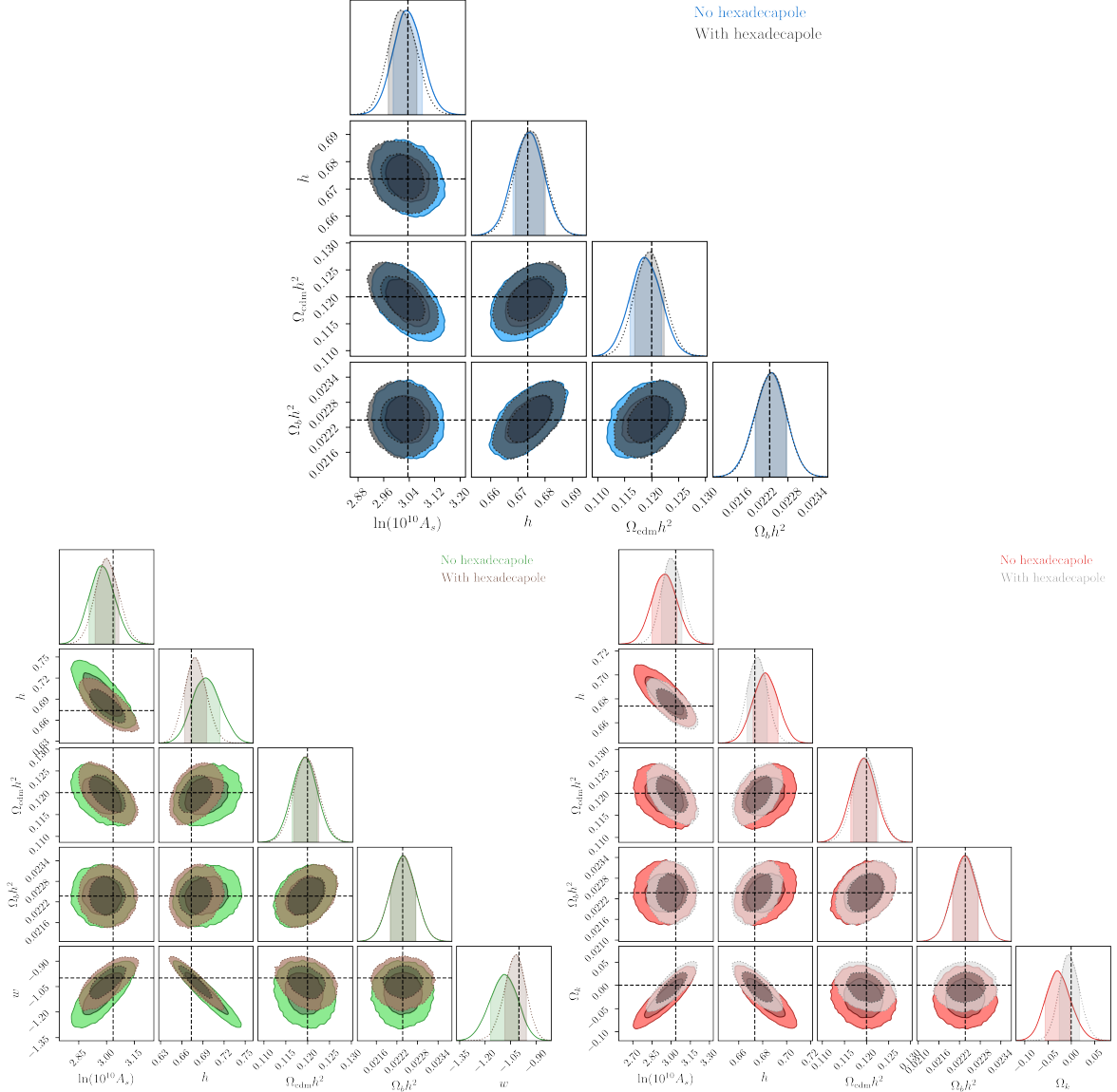


**Figure 10.** This plot shows the effect of adding hexadecapole on the constraints of cosmological parameters. Here, we use the combination of LRG, ELG, and QSO. Contrary to *ShapeFit*, including the hexadecapole does not improve the constraints of cosmological parameters for the  $\Lambda$ CDM model (top panel) probably because the internal prior of  $\Lambda$ CDM on the *Shapefit* parameters allows little information can be gained from the hexadecapole. However, for  $w$ CDM (lower left) and  $o$ CDM (lower right), the improvement from adding the hexadecapole is significant and reduces the systematic bias.



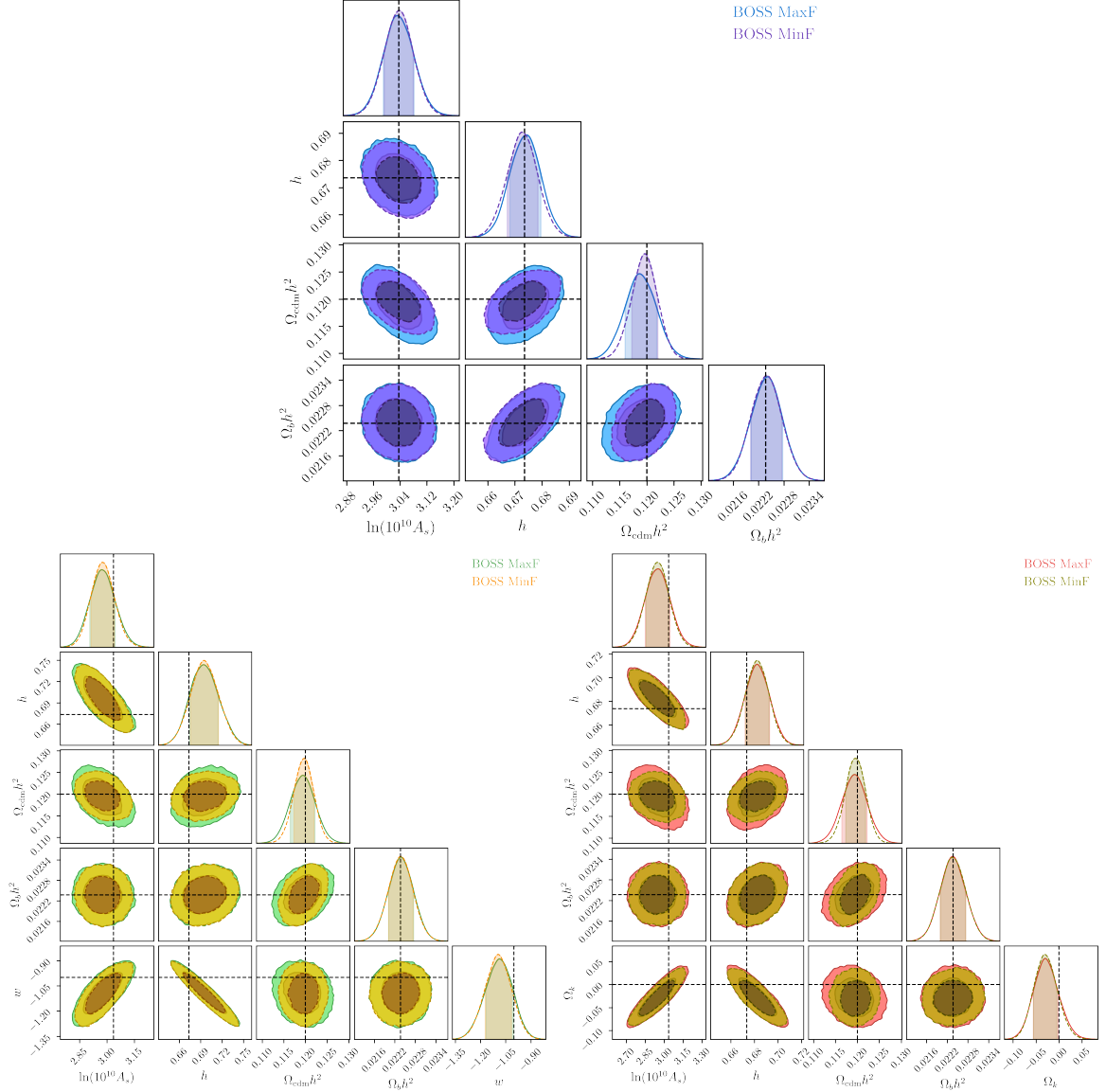


**Figure 11.** Cosmological constraints after changing the prior configuration from “BOSS MaxF” to “BOSS MinF” in *Full-Modelling* fitting. Both contours are produced using the combination of the LRG, ELG, and QSO mocks without the hexadecapole. Within  $\Lambda$ CDM (top panel),  $w$ CDM (lower left) and  $o$ CDM (lower right) the only impact is that the constraint on  $\omega_{\text{cdm}}$  is tighter than for the “BOSS MaxF” configuration. This is consistent with Fig. 6 where the constraint on the *ShapeFit* parameter  $m$  is tighter with the “BOSS MinF” configuration.

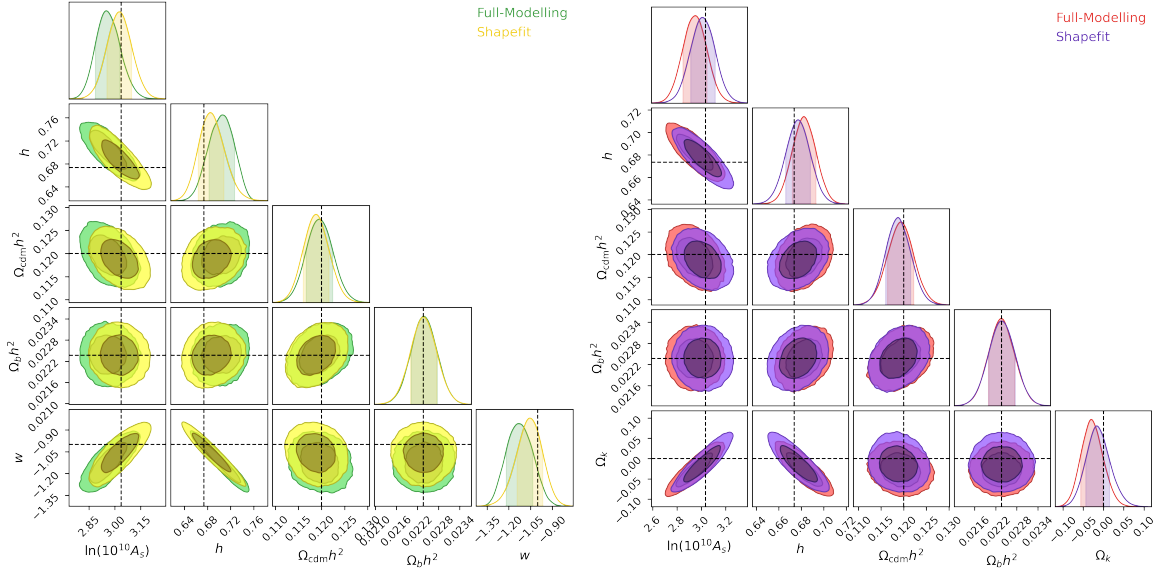


**Figure 12.** This figure compares the constraints from *ShapeFit* and *Full-Modelling* within the  $w$ CDM (left) and  $\Lambda$ CDM (right) cosmological models. The constraints are consistent with each other from both methods except for small shifts in the  $\ln(10^{10} A_s)$  and  $h$  parameters, which in turn propagate through into  $w$  and  $\Omega_k$ . This is similar to the shift of  $\ln(10^{10} A_s)$  in the  $\Lambda$ CDM model, propagates through the degeneracy direction.

the spherical Bessel transform of the linear, 1-loop, and counter-term power spectrum during the instantiation with FFTLOG [70].<sup>5</sup> These correlation function terms are added together in the same way as the power spectrum terms to compute the theoretical correlation function. Our aim here is simply to present that the model can also be easily and robustly applied to correlation function measurements — given the implementation in PYBIRD, we expect our findings for the power spectrum to propagate through to the correlation function and all that remains is to demonstrate that a good fit to the data can be obtained for a reasonable choice of fitting scales and that the constraints from the power spectrum and correlation function are consistent with each other.

To start, Fig. 13 shows the best-fit correlation function and the data correlation function for different choices of minimum fitting scale  $s_{\min}$  using the Full-Modelling approach. The best-fit correlation functions are consistent with each other for the monopole for  $s_{\min} = 30h^{-1}\text{Mpc}$  and  $s_{\min} = 42h^{-1}\text{Mpc}$ . However, the best-fit for  $s_{\min} = 22h^{-1}\text{Mpc}$  is constantly larger than the other two best-fits for the monopole and smaller than the other two best-fits for the quadrupole. This is driven by the small-scale data, which has much smaller error bars. This indicates our model starts to break down at small scales.

To explore this further, Fig. 14 and the corresponding Table 5 illustrate that generally increasing  $s_{\min}$  reduces the constraining power because we are losing information. Different from the power spectrum, the systematic error does not reduce when we remove small-scale information. This is because during the Fourier transform, the systematics from the small-scale can potentially leak into the large-scale. Therefore, increasing  $s_{\min}$  does not necessarily reduce the systematic bias. More importantly, this systematic bias could creep in around the

<sup>5</sup>The spherical Bessel transforms of the stochastic terms are extremely small, so they are ignored when fitting the correlation function.

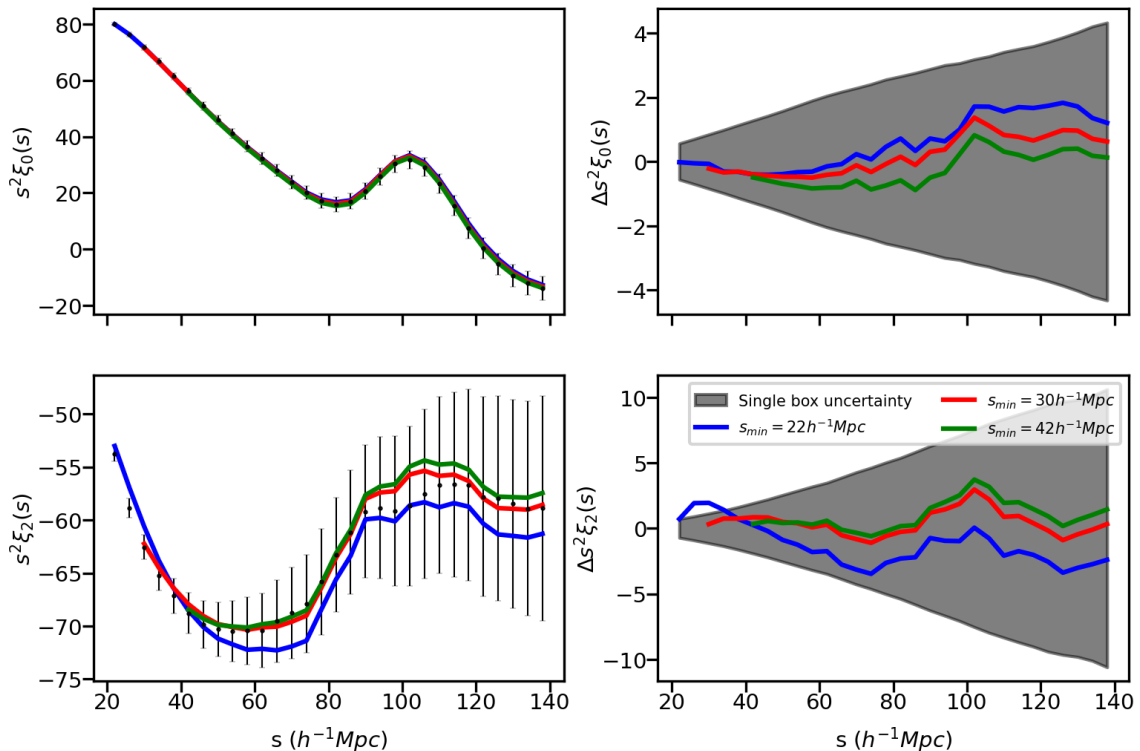


**Figure 13.** The best-fit correlation functions against the data. The error bars are given by the single-box covariance matrix. The grey band on the right corresponds to the error bars on the left. The best-fit correlation functions are consistent with each other for the monopole for  $s_{\min} = 30h^{-1}\text{Mpc}$  and  $s_{\min} = 42h^{-1}\text{Mpc}$ . However, the best-fit for  $s_{\min} = 22h^{-1}\text{Mpc}$  is consistently larger than the other two best-fits for the monopole and smaller than the other two best-fits for the quadrupole, arising from the fit being driven by the small-scale data which has smaller error bars.

BAO peak. Even though the position of BAO is extremely robustly predicted by theory, the shape, and damping are quite affected by non-linear physics, including the IR-resummation terms in the model. The systematics introduced by the Fourier transform could affect the constraints, particularly as intermediate scales are removed and the shape close to the BAO relies more and more on non-linear physics. This can be seen in Fig. 13 where in detail the model fails to predict the exact shape of the BAO in the quadrupole. This in turn suggests there is a ‘sweet spot’ of around  $s_{\min} = 30h^{-1}\text{Mpc}$  where the model is the most accurate.

Finally, in Fig. 15, we compare the constraints from the correlation function to the power spectrum for a similar range of scales. For the correlation function (power spectrum), we fix  $s_{\max} = 138h^{-1}\text{Mpc}$  ( $k_{\min} = 0.02h\text{Mpc}^{-1}$ ). For the top left plot, we set  $s_{\min} = 42h^{-1}\text{Mpc}$  ( $k_{\max} = 0.16h\text{Mpc}^{-1}$ ). For the top right plot, we set  $s_{\min} = 30h^{-1}\text{Mpc}$  ( $k_{\max} = 0.20h\text{Mpc}^{-1}$ ). For the bottom plot, we set  $s_{\min} = 22h^{-1}\text{Mpc}$  ( $k_{\max} = 0.28h\text{Mpc}^{-1}$ ). The  $s_{\min}$  and  $k_{\max}$  are chosen such that  $s_{\min} \approx \frac{2\pi}{k_{\max}}$ . This figure illustrates that the constraints of cosmological parameters within the  $\Lambda\text{CDM}$  from the correlation function are consistent with the constraints from the power spectrum. For our optimum choice of scales (the top right panel), the constraining power is similar, and there is only a small shift ( $< 0.5\sigma$ ) in the constraints primarily in the  $h$  and  $\ln(10^{10}A_s)$  parameters. We find that as one goes

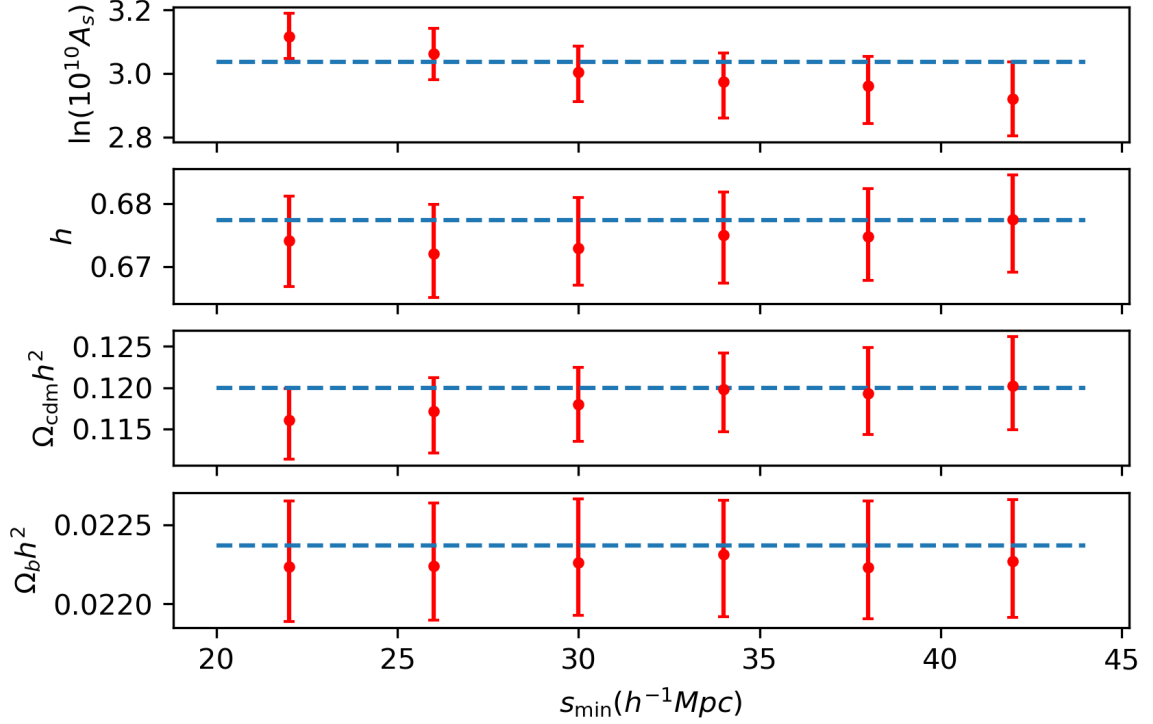


**Figure 14.** The effect of  $s_{\min}$  of the correlation function on the constraints of cosmological parameters within the  $\Lambda$ CDM cosmological model. Except for the prior dominated  $\omega_b$ , increasing  $s_{\min}$  generally reduces the constraining power because the information on the small-scale is lost. The systematic error doesn't reduce when removing small-scale information. We hypothesize this is because the small-scale systematics mixes with the large-scale information during the spherical Bessel transform. Furthermore, the inaccuracies in the modelling of the BAO shape and damping could also introduce bias on the large-scale. We find the most accurate model is obtained when  $s_{\min} = 30 h^{-1}\text{Mpc}$ .

**Table 5.** This table summarizes the deviation of the best-fits from the truth values for the correlation function with different  $s_{\min}$ . The deviations are generally smaller than  $1\sigma$  for all the scales we tested.

Model	$\Delta \ln(10^{10} A_s)\%$	$\Delta h\%$	$\Delta \Omega_{\text{cdm}} h^2\%$	$\Delta \Omega_b h^2\%$
$s_{\min} = 22h^{-1}\text{Mpc}$	$2.6^{+2.4}_{-2.3}$	$0.1^{+1.0}_{-1.1}$	$-3.2^{+3.1}_{-4.0}$	$-0.6^{+1.8}_{-1.6}$
$s_{\min} = 26h^{-1}\text{Mpc}$	$0.9^{+2.6}_{-2.7}$	$-0.2^{+1.2}_{-1.0}$	$-2.4^{+3.4}_{-4.2}$	$-0.6^{+1.8}_{-1.5}$
$s_{\min} = 30h^{-1}\text{Mpc}$	$-1.0^{+2.6}_{-3.1}$	$-0.11^{+1.20}_{-0.87}$	$-1.7 \pm 3.7$	$-0.5^{+1.8}_{-1.5}$
$s_{\min} = 34h^{-1}\text{Mpc}$	$-2.0^{+2.9}_{-3.8}$	$0.2^{+1.0}_{-1.1}$	$-0.1^{+3.7}_{-4.3}$	$-0.3^{+1.5}_{-1.8}$
$s_{\min} = 38h^{-1}\text{Mpc}$	$-2.5^{+3.1}_{-3.9}$	$0.2^{+1.1}_{-1.0}$	$-0.6^{+4.6}_{-4.1}$	$-0.6^{+1.9}_{-1.5}$
$s_{\min} = 42h^{-1}\text{Mpc}$	$-3.8 \pm 3.8$	$0.6^{+1.0}_{-1.2}$	$0.2^{+5.0}_{-4.4}$	$-0.4^{+1.7}_{-1.6}$

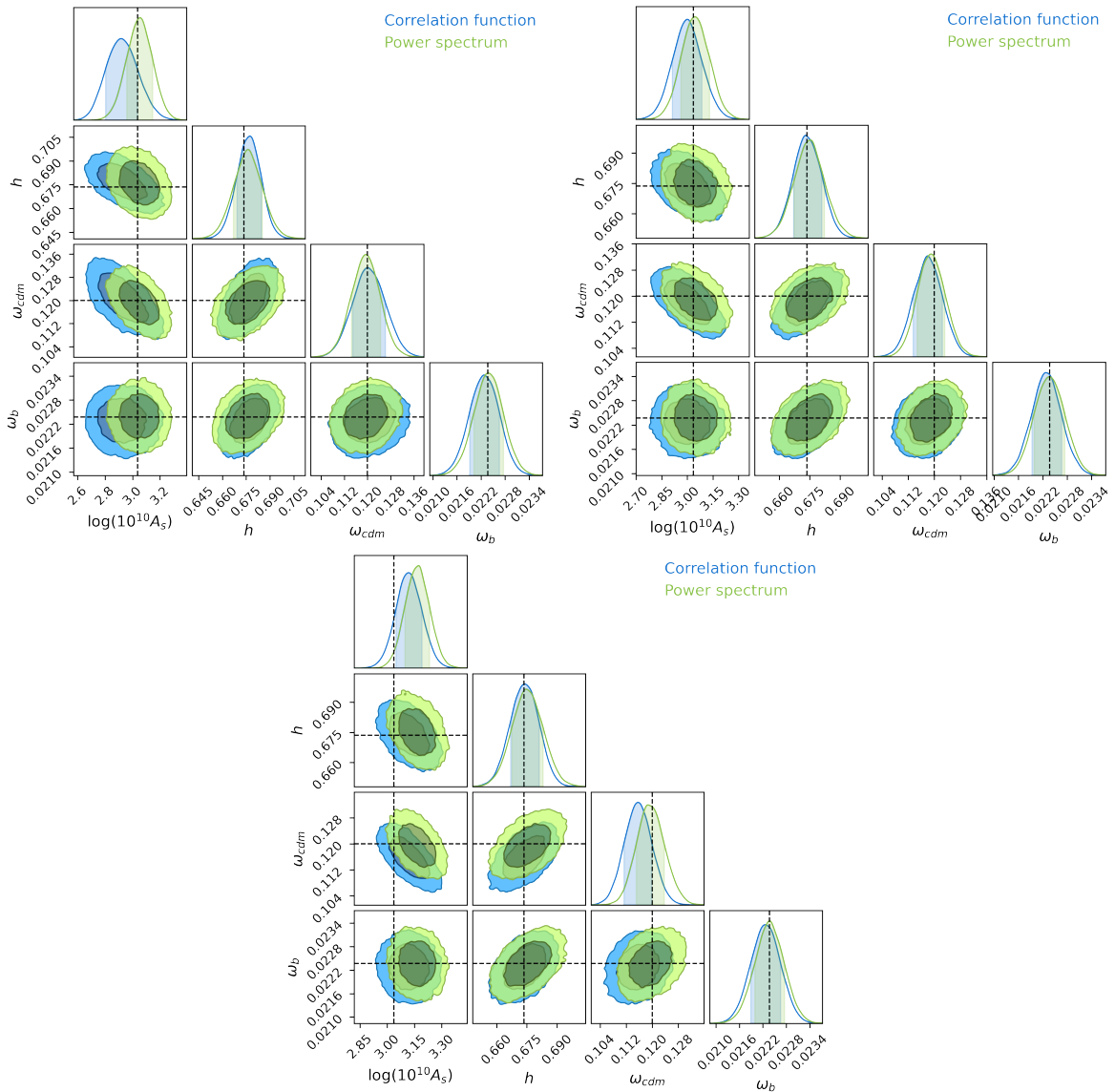


**Figure 15.** Comparing the constraints from correlation function and power spectrum. They both use the “BOSS MaxF” prior and without the hexadecapole. For all three figures,  $s_{\max} = 138h^{-1}\text{Mpc}$  for the correlation functions and  $k_{\min} = 0.02h\text{Mpc}^{-1}$  for the power spectra. On the top left, we use  $k_{\max} = 0.16h\text{Mpc}^{-1}$  for the power spectrum and  $s_{\min} = 42h^{-1}\text{Mpc}$  for the correlation function. On the top right, we use  $k_{\max} = 0.20h\text{Mpc}^{-1}$  for the power spectrum and  $s_{\min} = 30h^{-1}\text{Mpc}$  for the correlation function. On the bottom, we use  $k_{\max} = 0.28h\text{Mpc}^{-1}$  for the power spectrum and  $s_{\min} = 22h^{-1}\text{Mpc}$  for the correlation function. For all three plots, results from  $k_{\max} = 0.20h\text{Mpc}^{-1}$  and  $s_{\min} = 30h^{-1}\text{Mpc}$  are largely consistent with at most  $0.5\sigma$  shifts in the constraints, mainly where the power spectrum becomes biased more quickly when including small scales, or where the correlation function loses constraining power more quickly fitting to only larger scales.

to smaller scales, the correlation function tends to stay robust for longer than the power spectrum. Conversely, the correlation function loses constraining power more quickly as we cut to larger scales.

In summary, we expect consistent results from applying PYBIRD to the DESI data using either the correlation function or power spectrum. Although we have only tested the correlation function method with the LRG mocks, we expect similar consistency for other tracers and the combined probes since in our implementation the correlation function is treated purely as the Fourier counterpart of the power spectrum.

## 8 Conclusion

This work has thoroughly tested and validated that the PYBIRD EFTofLSS model and algorithm can produce unbiased tight constraints for the cosmological parameters for the DESI survey, and at a level of accuracy and precision sufficient for upcoming Year 1 analyses using the combination of LRG, ELG and QSO galaxy types that DESI is observing. We have implemented two different ways of extracting cosmological constraints using this model: *Full-Modelling* fitting of the data given a set of cosmological parameters, and the *ShapeFit* compression method. We find the constraints on cosmological parameters from both methods are remarkably consistent within the  $\Lambda$ CDM,  $w$ CDM,  $o$ CDM cosmological models, with only small ( $\simeq 0.3\sigma$ ) systematic shifts of best-fit cosmological parameters between *Full-Modelling* and *ShapeFit* analyses. This difference is small, and we will leave it for future work to investigate its origin.

In more detail, for both the *Full-Modelling* and *ShapeFit* methods we find that using a maximum fitting scale of  $k_{\max} = 0.20h\text{Mpc}^{-1}$  gives accurate constraints with the single box covariance (equivalent to DESI Y5 volume) — going beyond this does not substantially improve the constraining power of the model, and slightly increases the systematic errors. We also find that including the hexadecapole does not improve the constraints for the  $\Lambda$ CDM model, but gives a notable improvement on the constraints for the  $w$ CDM and the  $o$ CDM models. We also find a reduction in systematic bias when including the hexadecapole, and as such recommend including this when fitting DESI or other next-generation data.

We also test different choices of prior configurations and show that the “BOSS MinF” case where we use a minimal set of nuisance parameters and the local Lagrangian relation to fix the values of the non-linear galaxy bias parameters to functions of the linear bias can slightly reduce bias, and with a slightly improved error. Lastly, we also constrain the cosmological parameters with the correlation function. We find the constraints are consistent with the results from the power spectrum. Although the correlation function tends to remain more robust as we include smaller-scale information, it loses constraining power more quickly when restricted to large-fitting scales.

This work forms one in a series validating different cosmological fitting pipelines for use in the DESI survey. A comparison between PYBIRD and other pipelines in DESI is summarized in the companion paper [10], where we find that the results in this paper are generally reflected in the other pipelines and that PYBIRD is in good agreement with other methods and the level required for DESI Year 1 analyses. Future work will apply PYBIRD and the configurations investigated herein to the data from DESI.

“Monkey bias” parameter	PyBird	Velocileptor
$a_1^m$	$b_1$	$b_1^v + 1$
$b_3^m$	$\frac{2}{7}b_2$	$\frac{2}{7} + b_s^v$
$f_1^m$	$\frac{3}{21}b_3$	$\frac{42 - 145b_1^v - 21b_3^v + 630b_s^v}{441}$
$b_1^m$	$\frac{5}{7}(b_2 - b_4)$	$\frac{5}{7} + b_1^v + \frac{b_2^v}{2} - \frac{b_s^v}{3}$

**Table 6.** The conversion of bias parameters in VELOCILEPTOR and PYBIRD to the “Monkey bias” parameters. The superscript  $v$  indicates the bias parameters are from the VELOCILEPTOR.

## A Co-evolution of PyBird bias parameters

Bias parameters in different models of Large-Scale Structure can be transformed to one another using the “Monkey bias” parameters [71]. For other codes tested as part of the DESI validation program (such as VELOCILEPTOR and FOLPS $\nu$ ), local Lagrangian relations [68] between their bias parameters are used to provide tighter constraints on cosmological parameters. However, to the best of the authors’ knowledge, no such relation is known for bias expansion used in PYBIRD. To derive such relations, we here use the co-evolution relation in VELOCILEPTOR and transform it to PYBIRD bias parameters using the “Monkey bias” relations. The conversion is summarized in Table 6.

For the local Lagrangian relation in VELOCILEPTOR,  $b_3^v$  and  $b_s^v$  are set to zero. Therefore,

$$\begin{aligned}
b_1 &= b_1^v + 1 \\
b_2 &= \frac{7}{2}\left(\frac{2}{7} + b_s^v\right) = 1 \\
b_3 &= \frac{7(42 - 145b_1^v - 21b_3^v + 630b_s^v)}{441} = \frac{294 - 1015(b_1 - 1)}{441} \\
b_4 &= -\frac{7}{5}(b_1 - 1) - \frac{7}{10}b_2^v \tag{A.1}
\end{aligned}$$

After the conversion, the only two free parameters are  $b_1$  and  $b_2^v$ . To simplify the equations further, instead of putting priors on  $b_2^v$  and then computing the corresponding  $b_4$  during each iteration of the fitting, we instead decide to put a flat prior on  $b_4$  directly. The range of this flat prior is determined by the prior on  $b_1$  and  $b_2^v$  used in the VELOCILEPTOR companion paper [11].

## B *ShapeFit* conversion nuances

In converting *ShapeFit* constraints to cosmological parameters, we use equation (3.5), (3.6), (3.7), and (3.11). For the  $\alpha$  parameters and  $f\sigma_8$ , the conversion is straightforward from these expressions. However, for the slope parameter  $m$ , there are different ways one can calculate the “de-wiggled” transfer function (i.e., the transfer function of baryons and dark matter, but without the presence of BAO), so we want to make sure the final constraints on the cosmological parameters do not depend on how this is obtained.

Using the analytical Eisenstein-Hu transfer function [63] (hereon referred to as EH98) formulae have been suggested [32]. However, these fitting functions are not necessarily ac-

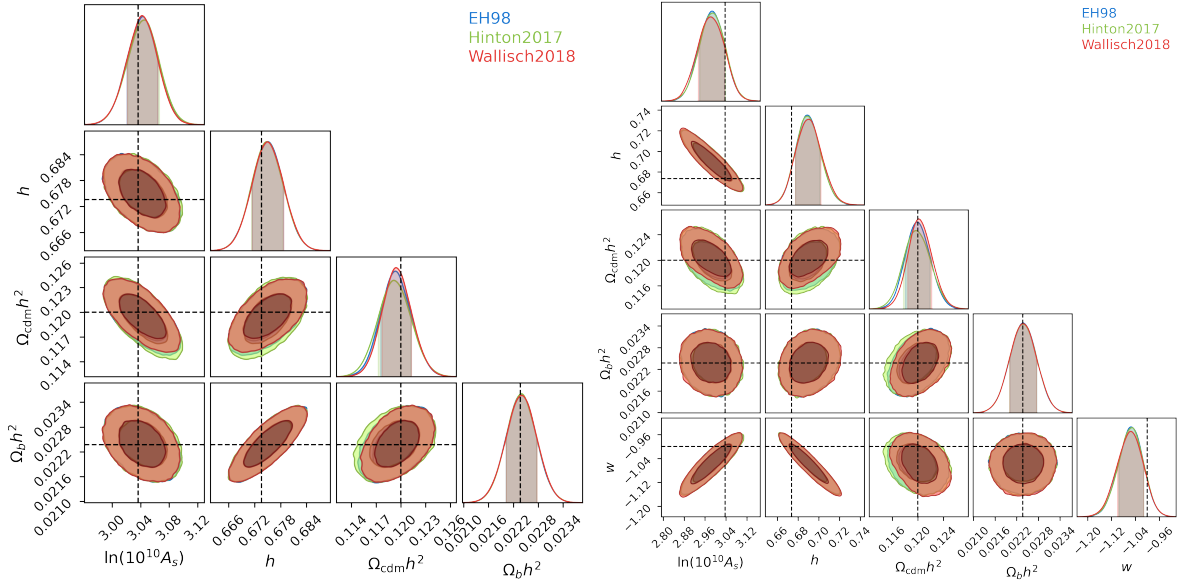


**Figure 16.** Different methods of calculating the no-wiggle linear power spectrum when converting from *ShapeFit* to cosmological parameters applied to the mean of the ELG mocks assuming the  $\Lambda$ CDM (left) and  $w$ CDM models. These fits are done with a  $25\times$  reduced covariance matrix to test whether different de-wiggle algorithms will introduce bias into the constraints of cosmological parameters. We find excellent agreements among all three methods for cosmological models.

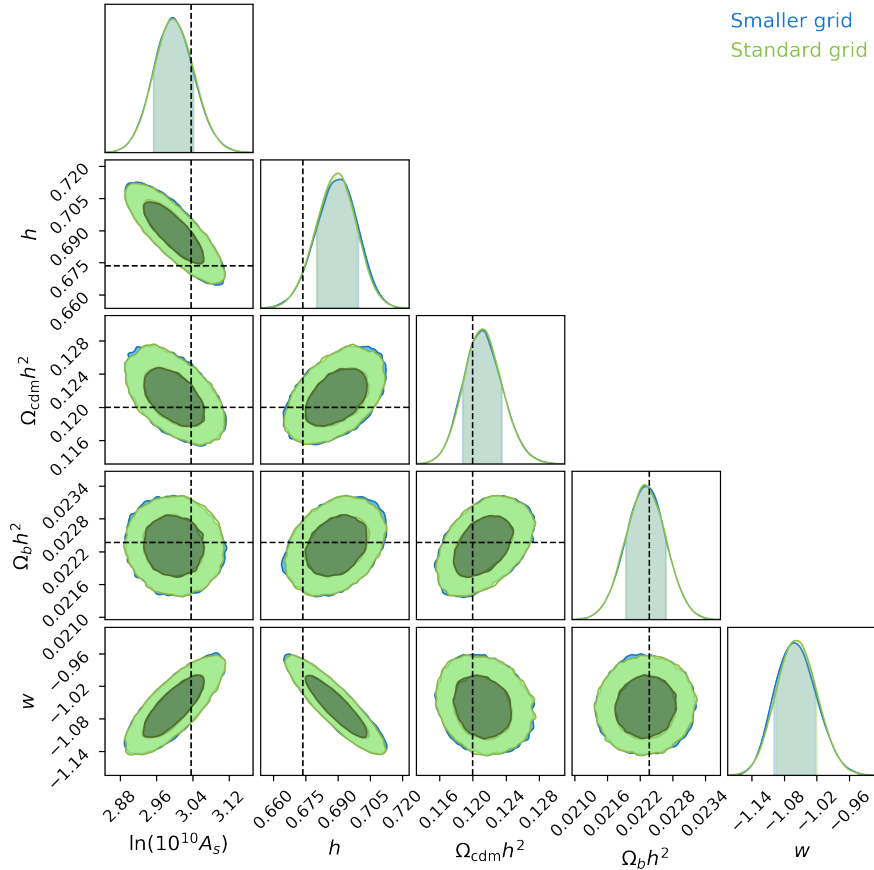
curate enough for modern cosmological inference, and numerical algorithms have been developed since then, particularly within the scope of BAO fitting. In this work, we also tested the polynomial algorithm from [64] (hereon referred to as Hinton2017) and spectral decomposition algorithm from [66] based on [65] (hereon referred to as Wallisch2018).

Fig. 16 compares the cosmological constraints obtained using these algorithms, within the context of the  $\Lambda$ CDM and  $w$ CDM models, to convert the *ShapeFit* parameters obtained from the mean of the ELG mocks with a  $25\times$  reduced covariance matrix. All three algorithms can give consistent constraints on the cosmological parameters. The Hinton2017 algorithm gives a slightly larger error bar for  $\Omega_{\text{cdm}}h^2$ , but this is not significant. Therefore, we conclude that our constraints on the cosmological parameters are independent of the de-wiggle algorithm used.

## C Performance of Taylor expansion

To speed up our fitting, we use a third-order Taylor expansion around a set of grid points to evaluate both the model power spectra and the *ShapeFit* parameters given a set of cosmological parameters. Here, we test whether the implementation of the Taylor expansion introduces any bias in our constraints on the cosmological parameters by changing the grid resolution used for pre-computing our models. The smaller grid size shrinks  $\Delta \ln(10^{10}A_s)$  from 0.25 to 0.05,  $\Delta h$  from 0.03 to 0.015,  $\Delta \omega_{\text{cdm}}h^2$  from 0.01 to 0.0025,  $\Delta \omega_b h^2$  from 0.001 to 0.0004, and  $\Delta w$  from 0.075 to 0.05. Fitting to the  $25\times$  reduced covariance matrix to provide a much more rigorous test, Fig. 17 illustrates that the grid size used for the Taylor expansion does not affect the constraints on the cosmological parameters in the  $w$ CDM model.





**Figure 17.** This plot shows the constraints on the  $w$ CDM cosmological parameters fitting to the mean of the LRG mocks with a  $25\times$  reduced covariance matrix for two very different choices of the Taylor expansion grid resolution. Compared to the standard grid size, the smaller grid size shrinks  $\Delta \ln 10^{10} A_s$  from 0.25 to 0.05,  $\Delta h$  from 0.03 to 0.015,  $\Delta \omega_{cdm}$  from 0.01 to 0.0025,  $\Delta \omega_b$  from 0.001 to 0.0004, and  $\Delta w$  from 0.075 to 0.05. Overall, we see that changing the size of the grid for Taylor expansion has no impact on the constraints of the cosmological parameters, indicating that the Taylor expansion does not introduce bias into our final constraints.

## D Marginalized vs unmarginalized constraints

Our results in this work have used analytic marginalization over linear order nuisance parameters to speed up the convergence of our fitting. By fitting the mean of the LRG mocks with a  $25\times$  reduced covariance matrix, Fig. 18 illustrates that the constraints on cosmological parameters both with and without analytic marginalization are consistent. This validates our use of the analytically marginalized likelihood to speed up the analysis.

## E Effect of different PyBird versions.

The version of PYBIRD we used is slightly different from the one in DESILIKE, which is used for DESI fitting. To understand whether different versions of PYBIRD will affect the cosmological constraints. We compare the constraints on the Shapefit parameters using two different versions of PYBIRD for LRG (top left), ELG (top right), and QSO (bottom). We find that the constraints are mostly consistent with each other. The DESILIKE version gives

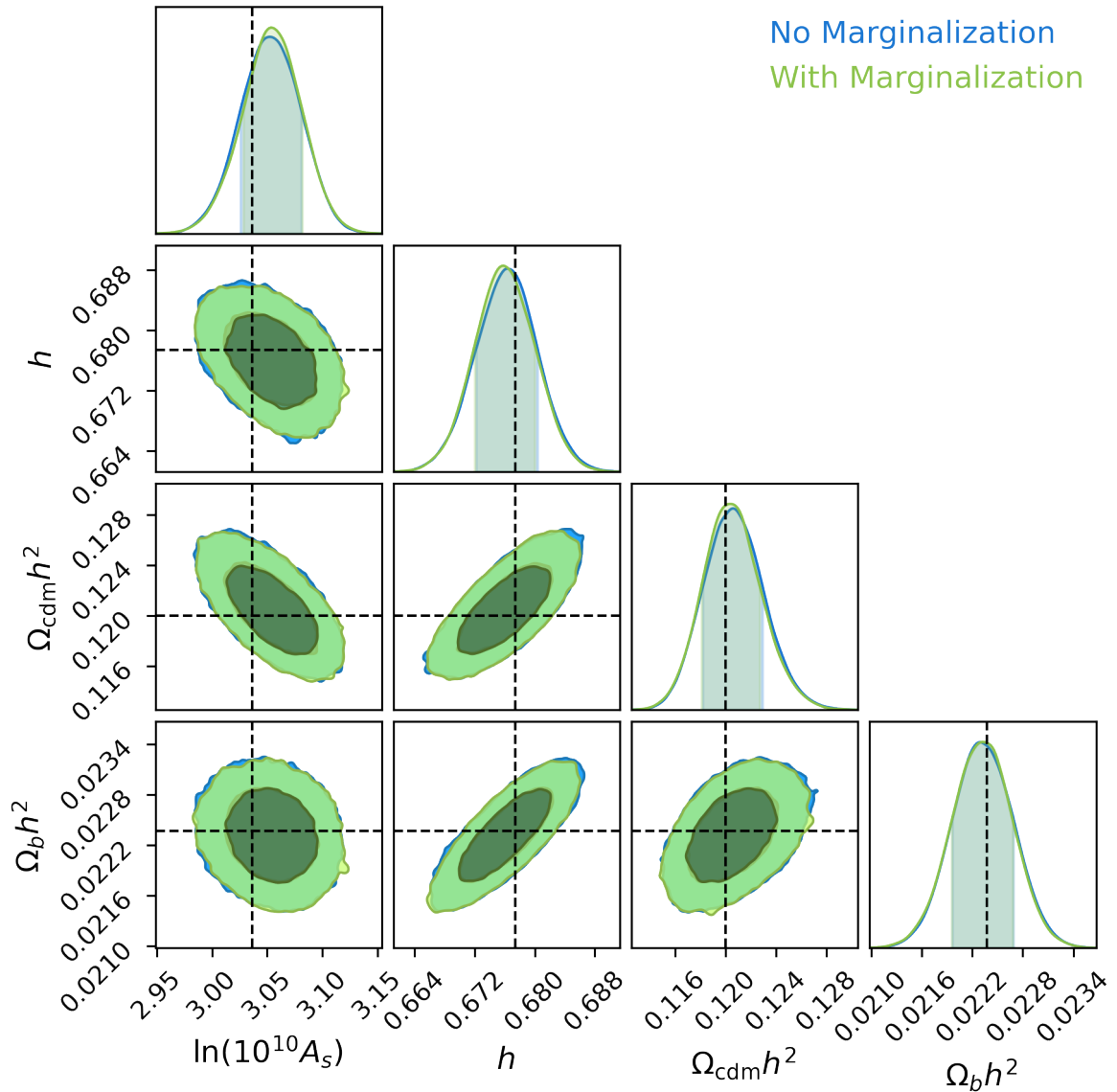


**Figure 18.** Parameter constraints with the mean of the LRG mocks and a  $25\times$  reduced covariance matrix using the analytically marginalized and unmarginalized likelihood functions. The constraints on the cosmological parameters from both methods are the same.

$\approx 5\%$  larger error bars for ELG and QSO. This is probably because  $k_r$  in DESILIKE is set to  $0.25h\text{Mpc}^{-1}$ , which is around three times smaller than in the latest version ( $0.70h\text{Mpc}^{-1}$ ). This means the prior on the counter terms in DESILIKE is larger than the latest version, so we see slightly weaker constraints.

## F Author affiliations

<sup>1</sup>School of Mathematics and Physics, The University of Queensland, QLD 4072, Australia.

<sup>2</sup>University of California, Berkeley, 110 Sproul Hall #5800 Berkeley, CA 94720, USA

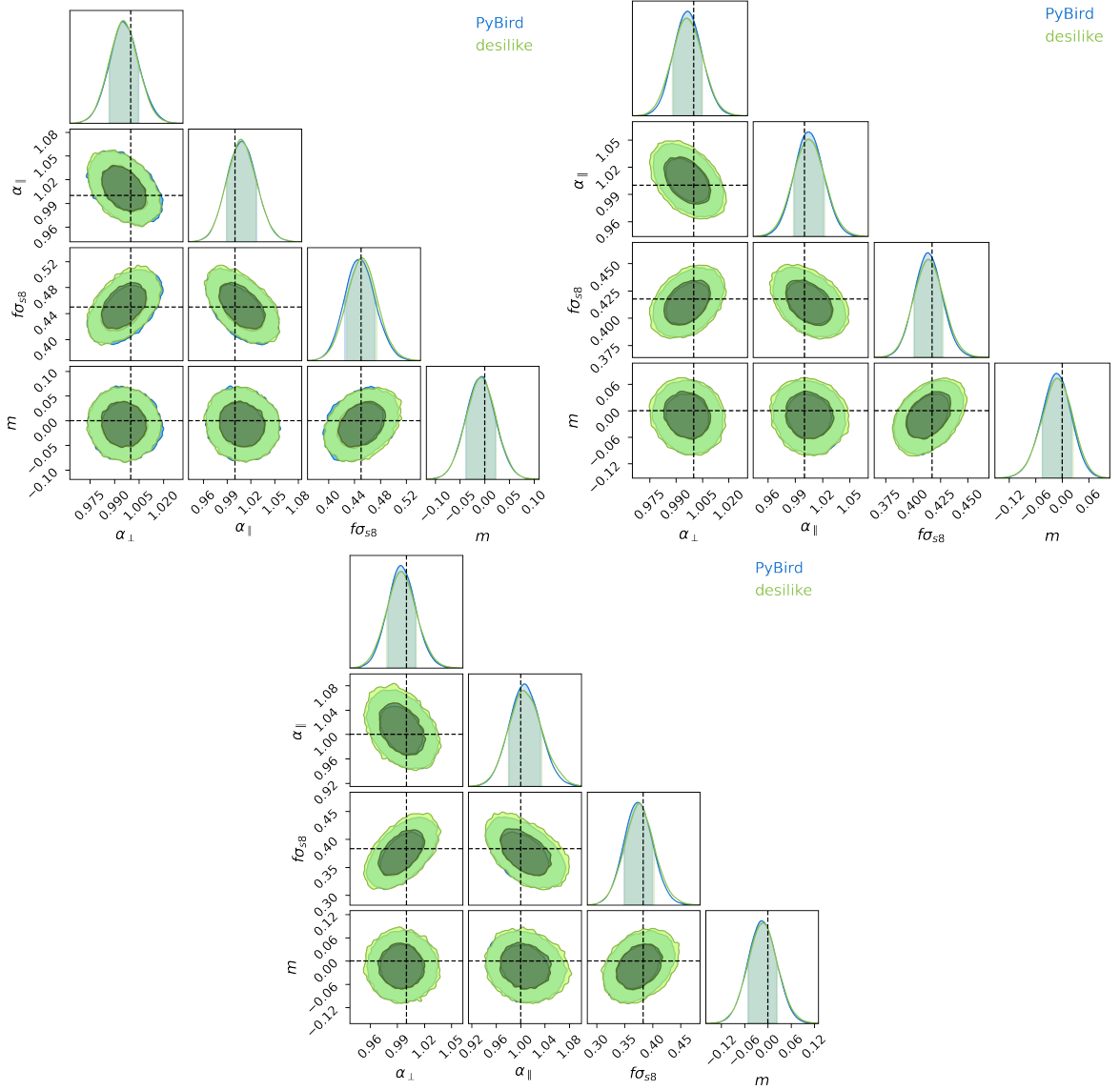


**Figure 19.** Compare constraints from my version of PYBIRD to the DESILIKE version for LRG (top left), ELG (top right), and QSO (bottom). They are mostly consistent with each other. The small difference is due to  $k_r$  in DESILIKE is much smaller, so the prior on the counter terms are larger in DESILIKE which weakens the constraints.

<sup>3</sup>Institut de Ciències del Cosmos (ICCUB), Universitat de Barcelona, Martí i Franquès, 1, E08028 Barcelona, Spain.

<sup>4</sup>Instituto de Ciencias Físicas, Universidad Nacional Autónoma de México, 62210, Cuernavaca, Morelos.

<sup>5</sup>Instituto de Física, Universidad Nacional Autónoma de México, Cd. de México C.P. 04510, México

<sup>6</sup>Sorbonne Université, Université Paris Diderot, Sorbonne Paris Cité, CNRS, Laboratoire de Physique Nucléaire et de Hautes Energies (LPNHE), 4 place Jussieu, F-75252, Paris Cedex 5, France

- <sup>7</sup>Lawrence Berkeley National Laboratory, 1 Cyclotron Road, Berkeley, CA 94720, USA
- <sup>8</sup>Physics Dept., Boston University, 590 Commonwealth Avenue, Boston, MA 02215, USA
- <sup>9</sup>University of Michigan, Ann Arbor, MI 48109, USA
- <sup>10</sup>Instituto Avanzado de Cosmología A. C., San Marcos 11 - Atenas 202. Magdalena Contreras, 10720. Ciudad de México, México
- <sup>11</sup>Department of Physics & Astronomy, University College London, Gower Street, London, WC1E 6BT, UK
- <sup>12</sup>Institute for Advanced Study, 1 Einstein Drive, Princeton, NJ 08540, USA
- <sup>13</sup>Department of Physics and Astronomy, The University of Utah, 115 South 1400 East, Salt Lake City, UT 84112, USA
- <sup>14</sup>Departamento de Física, Universidad de los Andes, Cra. 1 No. 18A-10, Edificio Ip, CP 111711, Bogotá, Colombia
- <sup>15</sup>Observatorio Astronómico, Universidad de los Andes, Cra. 1 No. 18A-10, Edificio H, CP 111711 Bogotá, Colombia
- <sup>16</sup>Institut d'Estudis Espacials de Catalunya (IEEC), 08034 Barcelona, Spain
- <sup>17</sup>Institute of Cosmology and Gravitation, University of Portsmouth, Dennis Sciama Building, Portsmouth, PO1 3FX, UK
- <sup>18</sup>Institute of Space Sciences, ICE-CSIC, Campus UAB, Carrer de Can Magrans s/n, 08913 Bellaterra, Barcelona, Spain
- <sup>19</sup>Center for Cosmology and AstroParticle Physics, The Ohio State University, 191 West Woodruff Avenue, Columbus, OH 43210, USA
- <sup>20</sup>Department of Physics, The Ohio State University, 191 West Woodruff Avenue, Columbus, OH 43210, USA
- <sup>21</sup>The Ohio State University, Columbus, 43210 OH, USA
- <sup>22</sup>NSF's NOIRLab, 950 N. Cherry Ave., Tucson, AZ 85719, USA
- <sup>23</sup>Departament de Física, Serra Húnter, Universitat Autònoma de Barcelona, 08193 Bellaterra (Barcelona), Spain
- <sup>24</sup>Institut de Física d'Altes Energies (IFAE), The Barcelona Institute of Science and Technology, Campus UAB, 08193 Bellaterra Barcelona, Spain
- <sup>25</sup>Institució Catalana de Recerca i Estudis Avançats, Passeig de Lluís Companys, 23, 08010 Barcelona, Spain
- <sup>26</sup>Department of Physics and Astronomy, University of Sussex, Brighton BN1 9QH, U.K
- <sup>27</sup>Departamento de Física, Universidad de Guanajuato - DCI, C.P. 37150, Leon, Guanajuato, México
- <sup>28</sup>Instituto Avanzado de Cosmología A. C., San Marcos 11 - Atenas 202. Magdalena Contreras, 10720. Ciudad de México, México
- <sup>29</sup>IRFU, CEA, Université Paris-Saclay, F-91191 Gif-sur-Yvette, France
- <sup>30</sup>Department of Physics and Astronomy, University of Waterloo, 200 University Ave W, Waterloo, ON N2L 3G1, Canada
- <sup>31</sup>Perimeter Institute for Theoretical Physics, 31 Caroline St. North, Waterloo, ON N2L 2Y5, Canada
- <sup>32</sup>Waterloo Centre for Astrophysics, University of Waterloo, 200 University Ave W, Waterloo, ON N2L 3G1, Canada
- <sup>33</sup>Space Sciences Laboratory, University of California, Berkeley, 7 Gauss Way, Berkeley, CA 94720, USA
- <sup>34</sup>Department of Physics, Kansas State University, 116 Cardwell Hall, Manhattan, KS 66506, USA

<sup>35</sup>Department of Physics and Astronomy, Sejong University, Seoul, 143-747, Korea

<sup>36</sup>CIEMAT, Avenida Complutense 40, E-28040 Madrid, Spain

<sup>37</sup>Department of Physics, University of Michigan, Ann Arbor, MI 48109, USA

<sup>38</sup>SLAC National Accelerator Laboratory, Menlo Park, CA 94305, USA

<sup>39</sup>National Astronomical Observatories, Chinese Academy of Sciences, A20 Datun Rd., Chaoyang District, Beijing, 100012, P.R. China

## G Data Availability

The data used in this analysis is available at <https://doi.org/10.5281/zenodo.10846264>. The version of the PYBIRD code in this paper is available at <https://github.com/pierrexyz/pybird/tree/desi>.

## Acknowledgments

We thank Arnaud de Mattia for implementing PYBIRD into the DESI pipelines and members of the Galaxy and Quasar Clustering working group within DESI for helpful discussions. We also thank Pierre Zhang for his helpful advice on PYBIRD.

YL and CH acknowledge support from the Australian Government through the Australian Research Council’s Laureate Fellowship (project FL180100168) and Discovery Project (project DP20220101395) funding schemes. YL is also supported by an Australian Government Research Training Program Scholarship. MM is supported by the DOE. HN is supported by Ciencia de Frontera grant No. 319359. SR and HN are supported by the Investigacion in Ciencia Basica CONAHCYT grant No. A1-S-13051 and PAPIIT IN108321 and IN116024, and Proyecto PIFF. HGM acknowledges support through the program Ramón y Cajal (RYC-2021-034104) of the Spanish Ministry of Science and Innovation. This research has made use of NASA’s Astrophysics Data System Bibliographic Services and the `astro-ph` pre-print archive at <https://arxiv.org/>, the `MATPLOTLIB` plotting library [72], and the `CHAINCONSUMER` and `EMCEE` packages [61, 73]. This research is done with the Getafix supercomputer at the University of Queensland and NERSC.

This material is based upon work supported by the U.S. Department of Energy (DOE), Office of Science, Office of High-Energy Physics, under Contract No. DE-AC02-05CH11231, and by the National Energy Research Scientific Computing Center, a DOE Office of Science User Facility under the same contract. Additional support for DESI was provided by the U.S. National Science Foundation (NSF), Division of Astronomical Sciences under Contract No. AST-0950945 to the NSF’s National Optical-Infrared Astronomy Research Laboratory; the Science and Technology Facilities Council of the United Kingdom; the Gordon and Betty Moore Foundation; the Heising-Simons Foundation; the French Alternative Energies and Atomic Energy Commission (CEA); the National Council of Humanities, Science and Technology of Mexico (CONAHCYT); the Ministry of Science and Innovation of Spain (MICINN), and by the DESI Member Institutions: <https://www.desi.lbl.gov/collaborating-institutions>. Any opinions, findings, and conclusions or recommendations expressed in this material are those of the author(s) and do not necessarily reflect the views of the U. S. National Science Foundation, the U. S. Department of Energy, or any of the listed funding agencies.

The authors are honored to be permitted to conduct scientific research on Iolkam Du’ag (Kitt Peak), a mountain with particular significance to the Tohono O’odham Nation.

## References

- [1] J.J.M. Carrasco, S. Foreman, D. Green and L. Senatore, *The effective field theory of large scale structures at two loops*, *Journal of Cosmology and Astroparticle Physics* **2014** (2014) 057.
- [2] R.A. Porto, L. Senatore and M. Zaldarriaga, *The lagrangian-space effective field theory of large scale structures*, *Journal of Cosmology and Astroparticle Physics* **2014** (2014) 022.
- [3] M. Levi, C. Bebek, T. Beers, R. Blum, R. Cahn, D. Eisenstein et al., *The DESI Experiment, a whitepaper for Snowmass 2013*, *arXiv e-prints* (2013) arXiv:1308.0847 [[1308.0847](#)].
- [4] DESI Collaboration, A. Aghamousa, J. Aguilar, S. Ahlen, S. Alam, L.E. Allen et al., *The DESI Experiment Part I: Science, Targeting, and Survey Design*, *arXiv e-prints* (2016) arXiv:1611.00036 [[1611.00036](#)].
- [5] DESI Collaboration, A. Aghamousa, J. Aguilar, S. Ahlen, S. Alam, L.E. Allen et al., *The DESI Experiment Part II: Instrument Design*, *arXiv e-prints* (2016) arXiv:1611.00037 [[1611.00037](#)].
- [6] DESI Collaboration, B. Abareshi, J. Aguilar, S. Ahlen, S. Alam, D.M. Alexander et al., *Overview of the Instrumentation for the Dark Energy Spectroscopic Instrument*, *AJ* **164** (2022) 207 [[2205.10939](#)].
- [7] DESI Collaboration, A.G. Adame, J. Aguilar, S. Ahlen, S. Alam, G. Aldering et al., *Validation of the Scientific Program for the Dark Energy Spectroscopic Instrument*, *AJ* **167** (2024) 62 [[2306.06307](#)].
- [8] DESI Collaboration, A.G. Adame, J. Aguilar, S. Ahlen, S. Alam, G. Aldering et al., *The Early Data Release of the Dark Energy Spectroscopic Instrument*, *arXiv e-prints* (2023) arXiv:2306.06308 [[2306.06308](#)].
- [9] DESI Collaboration, *DESI 2024 V: Analysis of the full shape of two-point clustering statistics from galaxies and quasars, in preparation* (2024) .
- [10] M. Maus, Y. Lai, H.E. Noriega, S. Ramirez-Solano, A. Aviles, S. Chen et al., *A comparison of effective field theory models of redshift space galaxy power spectra for desi 2024 and future surveys*, *arXiv e-prints* (2024) arXiv:2404.07272 [[2404.07272](#)].
- [11] M. Maus, S. Chen, M. White, J. Aguilar, S. Ahlen, A. Aviles et al., *An analysis of parameter compression and full-modeling techniques with Velocileptors for DESI 2024 and beyond*, *arXiv e-prints* (2024) arXiv:2404.07312 [[2404.07312](#)].
- [12] H.E. Noriega, A. Aviles, H. Gil-Marín, S. Ramirez-Solano, S. Fromenteau, M. Vargas-Magaña et al., *Comparing compressed and full-modeling analyses with folps: Implications for desi 2024 and beyond*, *arXiv e-prints* (2024) arXiv:2404.07269 [[2404.07269](#)].
- [13] S. Ramirez-Solano, M. Icaza-Lizaola, H.E. Noriega, M. Vargas-Magaña, S. Fromenteau, A. Aviles et al., *Full modeling and parameter compression methods in configuration space for desi 2024 and beyond*, *arXiv e-prints* (2024) arXiv:2404.07268 [[2404.07268](#)].
- [14] T. Colas, G. d'Amico, L. Senatore, P. Zhang and F. Beutler, *Efficient cosmological analysis of the SDSS/BOSS data from the effective field theory of large-scale structure*, *Journal of Cosmology and Astroparticle Physics* **2020** (2020) 001.
- [15] G. d'Amico, J. Gleyzes, N. Kokron, K. Markovic, L. Senatore, P. Zhang et al., *The cosmological analysis of the SDSS/BOSS data from the effective field theory of large-scale structure*, *Journal of Cosmology and Astroparticle Physics* **2020** (2020) 005.
- [16] G. D'Amico, L. Senatore and P. Zhang, *Limits on wcdm from the eftoflss with the pybird code*, *Journal of Cosmology and Astroparticle Physics* **2021** (2021) 006.
- [17] S.-F. Chen, Z. Vlah and M. White, *Consistent modeling of velocity statistics and redshift-space distortions in one-loop perturbation theory*, *Journal of Cosmology and Astroparticle Physics* **2020** (2020) 062.

- [18] S.-F. Chen, Z. Vlah, E. Castorina and M. White, *Redshift-space distortions in lagrangian perturbation theory*, *Journal of Cosmology and Astroparticle Physics* **2021** (2021) 100.
- [19] H.E. Noriega, A. Aviles, S. Fromenteau and M. Vargas-Magaña, *Fast computation of non-linear power spectrum in cosmologies with massive neutrinos*, *Journal of Cosmology and Astroparticle Physics* **2022** (2022) 038.
- [20] S. Ramirez, M. Icaza-Lizaola, S. Fromenteau, M. Vargas-Magaña and A. Aviles, *Full shape cosmology analysis from boss in configuration space using neural network acceleration*, 2023.
- [21] A.F. Heavens, R. Jimenez and O. Lahay, *Massive lossless data compression and multiple parameter estimation from galaxy spectra*, *Monthly Notices of the Royal Astronomical Society* **317** (2000) 965.
- [22] Y. Lai, C. Howlett and T.M. Davis, *Faster cosmological analysis with power spectrum without simulations*, 2023.
- [23] F. Beutler, H.-J. Seo, S. Saito, C.-H. Chuang, A.J. Cuesta, D.J. Eisenstein et al., *The clustering of galaxies in the completed SDSS-III baryon oscillation spectroscopic survey: anisotropic galaxy clustering in fourier space*, *Monthly Notices of the Royal Astronomical Society* **466** (2016) 2242.
- [24] J.N. Grieb, A.G. Sánchez, S. Salazar-Albornoz, R. Scoccimarro, M. Crocce, C.D. Vecchia et al., *The clustering of galaxies in the completed SDSS-III baryon oscillation spectroscopic survey: Cosmological implications of the fourier space wedges of the final sample*, *Monthly Notices of the Royal Astronomical Society* (2017) stw3384.
- [25] S. Satpathy, S. Alam, S. Ho, M. White, N.A. Bahcall, F. Beutler et al., *The clustering of galaxies in the completed SDSS-III baryon oscillation spectroscopic survey: on the measurement of growth rate using galaxy correlation functions*, *Monthly Notices of the Royal Astronomical Society* **469** (2017) 1369.
- [26] H. Gil-Marín, J.E. Bautista, R. Paviot, M. Vargas-Magaña, S. de la Torre, S. Fromenteau et al., *The completed SDSS-IV extended baryon oscillation spectroscopic survey: measurement of the BAO and growth rate of structure of the luminous red galaxy sample from the anisotropic power spectrum between redshifts 0.6 and 1.0*, *Monthly Notices of the Royal Astronomical Society* **498** (2020) 2492.
- [27] M. Maus, S.-F. Chen and M. White, *A comparison of template vs. direct model fitting for redshift-space distortions in BOSS*, *Journal of Cosmology and Astroparticle Physics* **2023** (2023) 005.
- [28] B. Yu, U. Seljak, Y. Li and S. Singh, *RSD measurements from BOSS galaxy power spectrum using the halo perturbation theory model*, *Journal of Cosmology and Astroparticle Physics* **2023** (2023) 057.
- [29] M. Vargas-Magaña, S. Ho, A.J. Cuesta, R. O'Connell, A.J. Ross, D.J. Eisenstein et al., *The clustering of galaxies in the completed SDSS-III baryon oscillation spectroscopic survey: theoretical systematics and baryon acoustic oscillations in the galaxy correlation function*, *Monthly Notices of the Royal Astronomical Society* **477** (2018) 1153.
- [30] P. Carter, F. Beutler, W.J. Percival, C. Blake, J. Koda and A.J. Ross, *Low redshift baryon acoustic oscillation measurement from the reconstructed 6-degree field galaxy survey*, *Monthly Notices of the Royal Astronomical Society* **481** (2018) 2371.
- [31] O.H. Philcox, B.D. Sherwin, G.S. Farren and E.J. Baxter, *Determining the hubble constant without the sound horizon: Measurements from galaxy surveys*, *Physical Review D* **103** (2021) .
- [32] S. Brieden, H. Gil-Marín and L. Verde, *ShapeFit: extracting the power spectrum shape information in galaxy surveys beyond BAO and RSD*, *Journal of Cosmology and Astro-Particle Physics* **2021** (2021) 054 [2106.07641].

- [33] S. Brieden, H. Gil-Marín and L. Verde, *A tale of two (or more) h's*, *Journal of Cosmology and Astroparticle Physics* **2023** (2023) 023.
- [34] S. Brieden, H. Gil-Marín and L. Verde, *Model-independent versus model-dependent interpretation of the SDSS-III BOSS power spectrum: Bridging the divide*, *Physical Review D* **104** (2021) .
- [35] DESI Collaboration, *DESI 2024 I: Data Release 1 of the Dark Energy Spectroscopic Instrument, in preparation* (2025) .
- [36] N.A. Maksimova, L.H. Garrison, D.J. Eisenstein, B. Hadzhiyska, S. Bose and T.P. Satterthwaite, *Abacussummit: A massive set of high-accuracy, high-resolution n-body simulations*, *Monthly Notices of the Royal Astronomical Society* **508** (2021) 4017.
- [37] L.H. Garrison, D.J. Eisenstein, D. Ferrer, N.A. Maksimova and P.A. Pinto, *The abacus cosmological n-body code*, *Monthly Notices of the Royal Astronomical Society* **508** (2021) 575.
- [38] B. Hadzhiyska, D. Eisenstein, S. Bose, L.H. Garrison and N. Maksimova, *Compasso: A new halo finder for competitive assignment to spherical overdensities*, *Monthly Notices of the Royal Astronomical Society* **509** (2021) 501.
- [39] C.-H. Chuang, F.-S. Kitaura, F. Prada, C. Zhao and G. Yepes, *EZmocks: extending the zel'dovich approximation to generate mock galaxy catalogues with accurate clustering statistics*, *Monthly Notices of the Royal Astronomical Society* **446** (2014) 2621.
- [40] and N. Aghanim, Y. Akrami, M. Ashdown, J. Aumont, C. Baccigalupi, M. Ballardini et al., *Planck 2018 results. vi. cosmological parameters*, *Astron. Astrophys.* **641** (2020) A6.
- [41] C. Yèche, N. Palanque-Delabrouille, C.-A. Claveau, D.D. Brooks, E. Chaussidon, T.M. Davis et al., *Preliminary Target Selection for the DESI Quasar (QSO) Sample*, *Research Notes of the American Astronomical Society* **4** (2020) 179 [2010.11280].
- [42] E. Chaussidon, C. Yèche, N. Palanque-Delabrouille, D.M. Alexander, J. Yang, S. Ahlen et al., *Target Selection and Validation of DESI Quasars*, *Astrophys. J.* **944** (2023) 107 [2208.08511].
- [43] R. Zhou, J.A. Newman, K.S. Dawson, D.J. Eisenstein, D.D. Brooks, A. Dey et al., *Preliminary target selection for the DESI luminous red galaxy (LRG) sample*, *Research Notes of the AAS* **4** (2020) 181.
- [44] R. Zhou, B. Dey, J.A. Newman, D.J. Eisenstein, K. Dawson, S. Bailey et al., *Target Selection and Validation of DESI Luminous Red Galaxies*, *AJ* **165** (2023) 58 [2208.08515].
- [45] A. Raichoor, D.J. Eisenstein, T. Karim, J.A. Newman, J. Moustakas, D.D. Brooks et al., *Preliminary Target Selection for the DESI Emission Line Galaxy (ELG) Sample*, *Research Notes of the American Astronomical Society* **4** (2020) 180 [2010.11281].
- [46] A. Raichoor, J. Moustakas, J.A. Newman, T. Karim, S. Ahlen, S. Alam et al., *Target selection and validation of DESI emission line galaxies*, *The Astronomical Journal* **165** (2023) 126.
- [47] J. Moon, D. Valcin, M. Rashkovetskyi, C. Saulder, J.N. Aguilar, S. Ahlen et al., *First detection of the bao signal from early desi data*, 2023.
- [48] A. Rocher, V. Ruhlmann-Kleider, E. Burtin, S. Yuan, A. de Mattia, A.J. Ross et al., *The desi one-percent survey: exploring the halo occupation distribution of emission line galaxies with abacussummit simulations*, 2023.
- [49] S. Yuan, H. Zhang, A.J. Ross, J. Donald-McCann, B. Hadzhiyska, R.H. Wechsler et al., *The desi one-percent survey: Exploring the halo occupation distribution of luminous red galaxies and quasi-stellar objects with abacussummit*, 2023.
- [50] Y.B. Zel'dovich, *Separation of uniform matter into parts under the action of gravitation.*, *Astrofizika* **6** (1970) 319.



- [51] J. Hartlap, P. Simon and P. Schneider, *Why your model parameter confidences might be too optimistic. unbiased estimation of the inverse covariance matrix*, *Astron. Astrophys.* **464** (2006) 399.
- [52] W.J. Percival, A.J. Ross, A.G. Sánchez, L. Samushia, A. Burden, R. Crittenden et al., *The clustering of galaxies in the SDSS-III baryon oscillation spectroscopic survey: including covariance matrix errors*, *Monthly Notices of the Royal Astronomical Society* **439** (2014) 2531.
- [53] E. Sellentin and A.F. Heavens, *Parameter inference with estimated covariance matrices*, *Monthly Notices of the Royal Astronomical Society: Letters* **456** (2015) L132–L136.
- [54] A. Perko, L. Senatore, E. Jennings and R.H. Wechsler, *Biased tracers in redshift space in the eft of large-scale structure*, 2016.
- [55] F. Bernardeau, S. Colombi, E. Gaztañaga and R. Scoccimarro, *Large-scale structure of the universe and cosmological perturbation theory*, *Physics Reports* **367** (2002) 1.
- [56] D. Blas, J. Lesgourgues and T. Tram, *The cosmic linear anisotropy solving system (CLASS). part II: Approximation schemes*, *Journal of Cosmology and Astroparticle Physics* **2011** (2011) 034.
- [57] A. Lewis and A. Challinor, “CAMB: Code for Anisotropies in the Microwave Background.” Astrophysics Source Code Library, record ascl:1102.026, Feb., 2011.
- [58] C. Howlett, A. Lewis, A. Hall and A. Challinor, *CMB power spectrum parameter degeneracies in the era of precision cosmology*, *Journal of Cosmology and Astroparticle Physics* **2012** (2012) 027.
- [59] T. Nishimichi, G. D’Amico, M.M. Ivanov, L. Senatore, M. Simonović, M. Takada et al., *Blinded challenge for precision cosmology with large-scale structure: Results from effective field theory for the redshift-space galaxy power spectrum*, *Physical Review D* **102** (2020) .
- [60] M. Lewandowski, L. Senatore, F. Prada, C. Zhao and C.-H. Chuang, *EFT of large scale structures in redshift space*, *Physical Review D* **97** (2018) .
- [61] S.R. Hinton, *ChainConsumer*, *The Journal of Open Source Software* **1** (2016) 00045.
- [62] N. Hand, Y. Feng, F. Beutler, Y. Li, C. Modi, U. Seljak et al., *nbodykit: An open-source, massively parallel toolkit for large-scale structure*, *The Astronomical Journal* **156** (2018) 160.
- [63] D.J. Eisenstein and W. Hu, *Power spectra for cold dark matter and its variants*, *The Astrophysical Journal* **511** (1999) 5.
- [64] S.R. Hinton, E. Kazin, T.M. Davis, C. Blake, S. Brough, M. Colless et al., *Measuring the 2d baryon acoustic oscillation signal of galaxies in WiggleZ: cosmological constraints*, *Monthly Notices of the Royal Astronomical Society* **464** (2016) 4807.
- [65] J. Hamann, S. Hannestad, J. Lesgourgues, C. Rampf and Y.Y. Wong, *Cosmological parameters from large scale structure - geometric versus shape information*, *Journal of Cosmology and Astroparticle Physics* **2010** (2010) 022–022.
- [66] B. Wallisch, *Cosmological probes of light relics*, .
- [67] R.J. Cooke, M. Pettini and C.C. Steidel, *One percent determination of the primordial deuterium abundance*, *The Astrophysical Journal* **855** (2018) 102.
- [68] V. Desjacques, D. Jeong and F. Schmidt, *Large-scale galaxy bias*, *Physics Reports* **733** (2018) 1.
- [69] C. Grove, C.-H. Chuang, N.C. Devi, L. Garrison, B. L’Huillier, Y. Feng et al., *The desi n-body simulation project i. testing the robustness of simulations for the desi dark time survey*, *Monthly Notices of the Royal Astronomical Society* **515** (2022) 1854.
- [70] M. Karamanis and F. Beutler, *hankl: A lightweight python implementation of the fftlog algorithm for cosmology*, 2021. 10.5281/ZENODO.4923137.

- [71] T. Fujita and Z. Vlah, *Perturbative description of biased tracers using consistency relations of LSS*, *Journal of Cosmology and Astroparticle Physics* **2020** (2020) 059.
- [72] J.D. Hunter, *Matplotlib: A 2d graphics environment*, *Computing in Science & Engineering* **9** (2007) 90.
- [73] D. Foreman-Mackey, D.W. Hogg, D. Lang and J. Goodman, *emcee: The mcmc hammer*, *Publications of the Astronomical Society of the Pacific* **125** (2013) 306.